



1 **Methane emissions from dairies in the Los Angeles Basin**

2

3 Camille Viatte¹, Thomas Lauvaux², Jacob K. Hedelius¹, Harrison Parker³, Jia Chen^{4,*}, Taylor Jones⁴,
4 Jonathan E. Franklin⁴, Aijun J. Deng², Brian Gaudet², Kristal Verhulst⁵, Riley Duren⁵, Debra
5 Wunch^{1,**}, Coleen Roehl¹, Manvendra K. Dubey², Steve Wofsy⁴, and Paul O. Wennberg¹

6

7 ¹Division of Geological and Planetary Sciences, California Institute of Technology, Pasadena, CA,
8 US

9 ²Department of Meteorology, Pennsylvania State University, University Park, PA, US

10 ³Earth System Observations, Los Alamos National Laboratory, Los Alamos, NM, US

11 ⁴School of Engineering and Applied Sciences, Harvard University, Cambridge, MA, US

12 ⁵Jet Propulsion Laboratory, California Institute of Technology, Pasadena, California, US

13 * Now at Electrical, Electronic and Computer Engineering, Technische Universtat of Munich,
14 Munich, Germany

15 ** Now at Department of Physics, University of Toronto, Toronto, ON, Canada



16 Abstract

17 We estimate the amount of methane (CH_4) emitted by the largest dairies in the southern
18 California region by combining measurements from four mobile solar-viewing ground-based
19 spectrometers (EM27/SUN), in situ isotopic $^{13/12}\text{CH}_4$ measurements from a CRDS analyzer
20 (Picarro), and a high-resolution atmospheric transport simulations with Weather Research and
21 Forecasting model in Large-Eddy Simulation mode (WRF-LES).

22 The remote sensing spectrometers measure the total column-averaged dry-air mole fractions of
23 CH_4 and CO_2 (X_{CH_4} and X_{CO_2}) in the near infrared region, providing information about total
24 emissions of the dairies at Chino. Gradients measured by the four EM27/SUN ranged from 0.2 to
25 22 ppb and from 0.7 to 3 ppm for X_{CH_4} and X_{CO_2} , respectively. To assess the fluxes of the dairies,
26 these gradient measurements are used in conjunction with the local atmospheric dynamics from
27 wind measurements at two local airports and from the WRF-LES simulations at 111 m resolution.

28 Our top-down CH_4 emissions derived using the Fourier Transform Spectrometers (FTS)
29 observations of 1.4 to 4.8 ppt/s are in the low-end of previous top-down estimates, consistent
30 with reductions of the dairy farms with urbanization in the domain. However, the wide range of
31 inferred fluxes points to the challenges posed by heterogeneity of the sources and meteorology.
32 Inverse modeling from WRF-LES is utilized to resolve the spatial distribution of CH_4 emissions in
33 the domain. Both the model and the measurements indicate heterogeneous emissions, with
34 contributions from anthropogenic and biogenic sources at Chino. A Bayesian inversion and a
35 Monte-Carlo approach are used to provide the CH_4 emissions of 3.2 to 4.7 ppt/s at Chino.

36 1) Introduction

37 Atmospheric methane (CH₄) concentration has increased by 150% since the pre-industrial era,
38 contributing to a global average change in radiative forcing of 0.5 W.m⁻² (Foster et al., 2007;
39 Myhre et al., 2013). Methane is naturally emitted by wetlands, but anthropogenic emissions now
40 contribute more than half of its total budget (Ciais et al., 2013), ranking it the second most
41 important anthropogenic greenhouse gas after carbon dioxide (CO₂).

42 The United Nations Framework Convention on Climate Change (UNFCCC,
43 <http://newsroom.unfccc.int/>) aims to reduce this CH₄ emission by reaching global agreements
44 and collective action plans. In the United States (US), the federal government aims to reduce CH₄
45 emissions by at least 17% below 2005 levels by 2020 by targeting numerous key sources such as
46 (in order of importance): agriculture, energy sectors (including oil, natural gas, and coal mines),
47 and landfills (Climate Action Plan, March 2014). Methane emissions are quantified using
48 “bottom-up” and “top down” estimates. The “bottom-up” estimates are based on scaling
49 individual emissions and process level information statistically (such as the number of cows,
50 population density or emission factor) with inherent approximations. “Top-down” estimates,
51 based on atmospheric CH₄ measurements, often differ from these reported inventories both in
52 the total emissions and the partitioning among the different sectors and sources (e.g. Hiller et
53 al., 2014). In the US, the disagreement in CH₄ emissions estimated can reach a factor of two or
54 more (Miller et al., 2013; Kort et al., 2014), and remains controversial regarding the magnitude
55 of emissions from the agricultural sector (Histov et al. 2014). Thus, there is an acknowledged
56 need for more accurate atmospheric measurements to verify the bottom-up estimates (Nisbet
57 and Weiss, 2010). This is especially true in urban regions, such as the Los Angeles basin, where
58 many different CH₄ sources (from farm lands, landfills, and energy sectors) are confined to a
59 relatively small area of ~87000 km² (Wunch et al., 2009; Hsu et al. 2010; Wennberg et al., 2012;
60 Peischl et al., 2013; Guha et al., 2015; Wong et al., 2015). Therefore, flux estimation at a local
61 scales is needed to resolve discrepancies between bottom-up and top-down approach and
62 improve apportion among CH₄ sources.



63 Inventories of CH₄ fluxes suggest that emissions from US agriculture increased by more than 10%
64 between 1990 and 2013 (Environmental Protection Agency, EPA, 2015), and by more than 20%
65 since 2000 in California (California Air Resources Board, CARB, 2015). In addition, these emissions
66 are projected to increase globally in the future due to increased food production (Tilman and
67 Clark, 2014). Livestock in California have been estimated to account for 63% of the total
68 agricultural emissions of greenhouse gases (mainly CH₄ and N₂O); dairy cows represented more
69 than 70% of the total CH₄ emissions from the agricultural sectors in 2013 (CARB, 2015). State-
70 wide actions are now underway to reduce CH₄ emissions from dairies (ARB concept paper, 2015).
71 Measurements at the local-scale with high spatial- and temporal-resolution are needed to assess
72 CH₄ fluxes associated with dairy cows and to evaluate the effectiveness of changing practices to
73 mitigate CH₄ emissions from agriculture.

74 Space-based measurements provide the dense and continuous datasets needed to constrain CH₄
75 emissions through inverse modeling (Streets et al., 2013). Recent studies have used the
76 Greenhouse gases Observing SATellite (GOSAT – footprint of ~10 km diameter) observations to
77 quantify mesoscale natural and anthropogenic CH₄ fluxes in Eurasia (Berchet et al., 2015) and in
78 the US (Turner et al., 2015). However, it is challenging to estimate CH₄ fluxes at smaller spatial
79 scales using satellite measurements due to their large observational footprint (Bréon and Ciais,
80 2010). Nevertheless, recent studies used the SCanning Imaging Absorption spectroMeter for
81 Atmospheric CHartography (SCIAMACHY – footprint of 60 km x 30 km) to assess emissions of a
82 large CH₄ point source in the US (Leifer et al., 2013; Kort et al., 2014).

83 Small-scale CH₄ fluxes are often derived from in situ measurements performed at the surface and
84 from towers (Zhao et al., 2009), and/or in situ and remote-sensing measurements aboard aircraft
85 (Karion et al., 2013; Peischl et al., 2013; Lavoie et al., 2015; Gordon et al., 2015). A recent study
86 emphasized the relatively large uncertainties of flux estimates from aircraft measurements using
87 the mass balance approach in an urban area (Cambaliza et al., 2014).

88 Ground-based solar absorption spectrometers are powerful tools that can be used to assess local
89 emissions (McKain et al., 2012). This technique has been used to quantify emissions from regional



90 to urban scales (Wunch et al., 2009; Stremme et al., 2013; Kort et al., 2014; Lindenmaier et al.,
91 2014; Hase et al., 2015; Franco et al., 2015, Wong et al., 2015, Chen et al., 2016).

92 In this study, we use four mobile ground-based total column spectrometers (called EM27/SUN,
93 Gisi et al., 2012) to estimate CH₄ fluxes from the largest dairy-farming area in the South Coast Air
94 Basin (SoCAB), located in the city of Chino, in San Bernardino County, California. The Chino area
95 was once home to one of the largest concentrations of dairy farms in the United States (US),
96 however rapid land-use change in this area may have caused CH₄ fluxes from the dairy farms
97 change rapidly in both space and time. Chen et al. (2016) used differential column measurements
98 (downwind minus upwind column gradient ΔX_{CH_4} across Chino) on a high-wind data to verify
99 emissions reported in the literature. In this study, the same column measurement network is
100 employed in conjunction with meteorological data and a high-resolution model to estimate CH₄
101 emissions at Chino for several different days, including more typical wind conditions.

102 In section 2 of this paper, the January 2015 field campaign at Chino is described, with details
103 about the mobile column and in situ measurements. In section 3, we describe the new high
104 resolution Weather Research & Forecasting (WRF) model with Large Eddy Simulations (LES)
105 setup. In section 4, results of CH₄ fluxes estimates are examined. Limitations of this approach, as
106 well as suggested future analyses are outlined in section 5.

107 2) Measurements in the Los Angeles Basin dairy farms108 2.1) Location of the farms: Chino, California

109 Chino (34.02°N, -117.69°W) is located in the eastern part SoCAB, called the Inland Empire, and
110 has historically been a major center for dairy production. With a growing population and
111 expanding housing demand, the agricultural industry has shrunk in this region and grown in the
112 San Joaquin Valley (California Central Valley). The number of dairies decreased from ~400 in the
113 1980's to 95 in 2013 (red area of panels a, b, and c in Figure 1). Nevertheless, in 2013 ~90 % of
114 the southern California dairy cow population (California Agricultural Statistics, 2013) remained
115 within the Chino area of ~6 x 9 km (Figure 1). These feedlots are a major point source of CH₄ in
116 the Los Angeles basin (Peischl et al., 2013).

117 2.2) Mobile column measurements: EM27/SUN

118 Atmospheric dry-air mole fractions of CH₄ and CO₂ (denoted X_{CH₄} and X_{CO₂}, Wunch et al., 2011)
119 have been measured using four ground-based mobile Fourier Transform Spectrometers (FTS).
120 The mobile instruments were purchased from Bruker Optics, are all EM27/SUN models. The four
121 FTS (two owned by Harvard University, denoted Harvard 1 and 2, one owned by Los Alamos
122 National Laboratory, denoted LANL, and one owned by the California Institute of Technology,
123 denoted Caltech, were initially gathered at the California Institute of Technology in Pasadena,
124 California in order to compare them against the existing Total Carbon Column Observing Network
125 (TCCON, Wunch et al., 2011) station and to each other, over several full days of observation. The
126 instruments were then deployed to Chino to develop a methodology to estimate greenhouse
127 gas emissions and improve the uncertainties on flux estimates from this major local source.
128 Descriptions of the capacities and limitations of the mobile EM27/SUN instruments have been
129 published in Chen et al. (2016) and Hedelius et al. (2016). For this analysis, we need to ensure
130 that all the data from the EM27/SUN instruments are on the same scale. Here, we reference all
131 instruments to the Harvard2 instrument. Standardized approaches (retrieval consistency,
132 calibrations between the instruments) are needed to monitor small atmospheric gradients using
133 total column measurements from the EM27/SUN. Indeed we ensured all retrievals used the same



134 algorithm, calibrated pressure sensors, and were scaled according to observed, small systematic
135 differences to reduce instrumental biases (Hedelius et al., 2016).

136 These modest resolution (0.5 cm^{-1}) spectrometers are equipped with solar-trackers (Gisi et al.,
137 2011) and measure throughout the day. To retrieve atmospheric total column abundances of
138 CH_4 , CO_2 , and oxygen (O_2) from these Near InfraRed (NIR) solar absorption spectra, we used the
139 GGG software suite, version GGG2014 (Wunch et al., 2015). Column measurements at Chino
140 were obtained on five days: the 15th, 16th, 22nd and 24th of January, and the 13th of August, 2015.
141 Of these days, January 15th, 16th, and 24th are sufficiently cloud-free for analysis. These days have
142 different meteorological conditions (i.e. various air temperatures, pressures, wind speeds and
143 directions), improving the representativeness of the flux estimates at Chino.

144 Figure 1 shows measurements made on January 15th, 16th, and 24th. Wind speeds and directions,
145 shown in the bottom panels of Figure 1, are measured at the two local airports inside the domain
146 (the Chino airport indicated on panels d, e, and f and the Ontario airport on panels g, h, and i).
147 Wind measurements from these two airports, located at less than 10 km apart, are made at an
148 altitude of 10 meters above the surface. The exact locations of the four EM27/SUN (colored
149 symbols in Figure 1 in the upper panels a, b, and c) were chosen each morning of the field
150 campaign to optimize the chance of measuring upwind and downwind of the plume. On the 15th
151 and 16th of January, the wind speed was low with a maximum of 3 ms^{-1} and highly variable
152 direction all day (Figure 1, panels d, e, g and h), therefore the four EM27/SUN were placed at
153 each corner of the source area to ensure that the plume was detected by at least one of the
154 instruments throughout the day. On the contrary, the wind in January 24th had a constant
155 direction from the Northeast and was a relatively strong $8\text{-}10 \text{ ms}^{-1}$ (Figure 1, panels f and i), so
156 the instruments were located such that one spectrometer (Harvard2) was always upwind (blue
157 symbols in Figure 1) and the others are downwind of the plume and at different distances from
158 the sources (black, green, and red symbols in Figure 1).

159 2.3) In situ measurements: Picarro

160 The EM27/SUN column measurements are supplemented by ground-based in situ measurement
161 using a commercial Picarro instruments during January campaign. The Picarro instruments use a



162 Cavity Ringdown Spectroscopy (CRDS) technique that employs a wavelength monitor and
163 attenuation to characterize species abundance.

164 In situ $^{12}\text{CH}_4$, CO_2 , and $^{13}\text{CH}_4$ measurements were performed on January 15th, 16th, and 22nd, and
165 August 13th 2015 at roughly 2m away from the LANL EM27/SUN (Figure 1 a, b, and c) with a
166 Picarro G2132-I instrument (Arata et al., 2016,
167 http://www.picarro.com/products_solutions/isotope_analyzers/). This Picarro, owned by LANL,
168 utilize a 1/4" synflex inlet tube placed approximately 3m above ground level to sample air using
169 a small vacuum pump. Precisions on $^{12}\text{CH}_4$, CO_2 , and $^{13}\text{CH}_4$ measurements are 6 ppb, 2 ppm, and
170 0.6 ‰, respectively.

171 To locate the major CH_4 sources in the dairy farms area, a second Picarro G2401 instrument
172 (http://www.picarro.com/products_solutions/trace_gas_analyzers/) from the Jet Propulsion
173 Laboratory (JPL) was deployed on January 15th, 2015. Precision on CH_4 measurements is ~1 ppb.

174 3) Model simulations175 3.1) Description of WRF-LES model

176 The Weather Research and Forecasting (WRF) model (Skamarock et al., 2008) is an atmospheric
177 dynamics model used for both operational weather forecasting, and scientific research
178 throughout the global community. Two key modules that supplement the baseline WRF system
179 are used here. First, the chemistry module WRF-Chem (Grell et al., 2005) adds the capability of
180 simulating atmospheric chemistry among various suites of gaseous and aerosol species. In this
181 study, CH₄ is modeled as a passive tracer because of its long life time relative to the advection
182 time at local scales. The longest travel time from the emission source region to the instrument
183 locations is less than an hour, which is extremely short compared to the lifetime of CH₄ in the
184 troposphere (~9 years). Therefore, no specific chemistry module is required. The version of WRF-
185 Chem used here (Lauvaux et al., 2012) allowed for the offline coupling between the surface
186 emissions, prescribed prior to the simulation, and its associated atmospheric tracers. Second, we
187 make use of the Large Eddy Simulation (LES) version of WRF (Moeng et al., 2007) on a high-
188 resolution model grid with 111-m horizontal grid spacing. A key feature of the simulation is the
189 explicit representation of the largest turbulent eddies of the Planetary Boundary Layer (PBL) in a
190 realistic manner. The more typical configuration of WRF (and other atmospheric models) is to be
191 run at a somewhat coarser resolution that is incapable of resolving PBL eddies. An advantage in
192 this study is that the integrated effect of all PBL eddies on vertical turbulent transport is
193 parameterized. By having a configuration with the combination of CH₄ tracers and PBL eddies,
194 we can realistically predict the evolution of released material at scales on the order of the PBL
195 depth or smaller.

196 In this real case experiment, the model configuration consists of a series of four one-way nested
197 grids, shown in Figure 2 and described further in the supplementary information section (S1).
198 Each domain contains 201 x 201 mass points in the horizontal, with 59 levels from the surface to
199 50 hPa, and the horizontal grid spacings are 3 km, 1 km, 333 m, and 111 m. All four domains use
200 the WRF-Chem configuration. The model 3-km, 1-km, and 333-m grids are run in the conventional
201 mesoscale configuration with a PBL parameterization, whereas the 111-m grid physics is LES. The



202 initial conditions for the cases are derived from the National Centers for Environmental
203 Prediction (NCEP) 0.25-degree Global Forecasting System (GFS) analysis fields (i.e., 0-hour
204 forecast) at 6-hour intervals. The simulations are performed from 12:00 to 00:00 UTC (= 04:00 to
205 16:00 LT) only, which corresponds to daylight hours when solar heating of the surface is present
206 and measurements are made.

207 Data assimilation is performed using Four Dimensional Data Assimilation (FDDA; Deng et al.,
208 2009) for the 3-km and 1-km domains. The assimilation improves the model performance
209 significantly (Rogers et al., 2013) without interfering with mass conservation and the continuity
210 of the air flow. Surface wind and temperature measurements, including from the Ontario (KONT)
211 and Chino (KCNO) airport stations, and upper-air measurements were assimilated within the
212 coarser grids using the WRF-FDDA system. However, no observations of any kind were
213 assimilated within the 333-m and 111-m domains; therefore, the influence of observations can
214 only come into these two domains through the boundary between the 333-m and 1-km grids.
215 Wind measurements at fine scale begin to resolve the turbulent perturbations, which would
216 require an additional pre-filtering. These measurements are used to evaluate the WRF model
217 performances at high resolutions.

218 Based on the terrain elevation in the LES domain (Figure 2), target emissions are located in a
219 triangular-shaped valley with the elevation decreasing gradually towards the South. However,
220 hills nearly surround the valley along the southern perimeter. Meanwhile, the foothills of the San
221 Gabriel Mountains begin just off the 111-m domain boundary to the North. As a result, the wind
222 fields in the valley are strongly modified by local topography, and can be quite different near the
223 surface than at higher levels.

224 3.2) Atmospheric inversion methodology: Bayesian framework and Simulated 225 Annealing error assessment

226 Due to the absence of an adjoint model in Large Eddy Simulation mode, the inverse problem is
227 approached with Green's functions, which correspond to the convolution of the Chino dairies
228 emissions and the WRF-LES model response. For the two simulations (January 15th and 16th), 16
229 rectangular areas of 2 x 2 km² (Figure 2) are defined across the feedlots to represent the state



230 vector (x) and therefore the spatial resolution of the inverse emissions, which correspond to the
231 entire dairy farms area of about $8 \times 8 \text{ km}^2$ once combined together. The 16 emitting areas
232 continuously release a known number of CH_4 molecules (prior estimate) during the entire
233 simulations, along with 16 individual tracers representing the 16 areas of the dairies area. The
234 final relationship between each emitting grid-cell and each individual measurement location is
235 the solution to the differential equation representing the sensitivity of each column
236 measurement to the different $2 \times 2 \text{ km}^2$ areas. The WRF-LES results are sampled every 10 minutes
237 at each sampling location to match the exact measurement times and locations of the EM27/SUN
238 instruments.

239 The inversion of the emissions over Chino is performed using a Bayesian analytical framework,
240 described by the following equation:

$$241 \quad x = x_0 + BH^T (HBH^T + R)^{-1} (y - Hx_0) \quad (1)$$

242 with x the inverse emissions, x_0 the prior emissions, B the prior emission error covariance, R the
243 observation error covariance, H the Green's functions, and y the observed column dry air mole
244 fractions. The dimension of the state vector is 16, assuming constant CH_4 emissions for each
245 individual day. Two maps of 16 emission estimates are produced corresponding to the $2 \times 2 \text{ km}^2$
246 areas for the two days (January 15th and 16th). A combined inversion provides a third estimate of
247 the emissions using 10-minute average column data from both days. The definition of the prior
248 error covariance matrix B is most problematic because little is known about the dairy farms
249 emissions except the presence of cows distributed in lots of small sizes. However, we assumed
250 no error correlation as it is known that cows are not distributed randomly across Chino. For the
251 definition of the variances in B , no reliable error estimate is available. The lack of error estimate
252 impacts directly the inverse emissions, therefore results in the generation of unreliable posterior
253 error estimates. Instead, we develop a Monte-Carlo approach using a Simulated Annealing (SA)
254 technique. We test the initial errors in the emissions by creating random draws with an error of
255 about 200% compared to the expected emissions (based on the dairy cows' emissions from CARB
256 2015). We then generate populations of random solutions and iterated 2000 times with the
257 Simulated Annealing algorithm. The metric used to select the best solutions is the Mean Absolute



258 Error (or absolute differences) between the simulated and observed column fractions. We store
259 the solutions exhibiting a final mismatch of less than 0.01 ppm to minimize the mismatch
260 between observed and simulated column fractions. The optimal solution and the range of
261 accepted emission scenarios are shown in Figure S2. The space of solutions provide a range of
262 accepted emissions for each 2 x 2 km² area that can be used as a confidence interval in the
263 inversion results. The posterior emissions from the Bayesian inversion are then compared to the
264 confidence interval from the Simulated Annealing to evaluate our final inverse emissions
265 estimates and the posterior uncertainties. The results are presented in Section 4.3.



266 4) Results

267 4.1) Observations of X_{CH_4} and X_{CO_2} in the dairy farms

268 Figure 3 shows the 1-minute average time series of X_{CH_4} (upper panels a, b, and c) and X_{CO_2} (d, e,
269 and f) derived from the four EM27/SUN. For days with slow wind, i.e. on January 15th and 16th
270 (Figure 1, panels d, e, g and h), the maximum gradients observed between the instruments are
271 17 and 22 ppb (parts per billion), and 2 and 3 ppm (parts per million), for X_{CH_4} and X_{CO_2} ,
272 respectively. Assuming that the observed Xgas changes are confined to the PBL, gradients in this
273 layer are about ten times larger. Gradients observed on January 15th and 16th are higher than
274 those of X_{CH_4} and X_{CO_2} of 2 ppb and 0.7 ppm observed on a windy day, the 24th. The X_{CH_4} and X_{CO_2}
275 variabilities captured by the instruments are due to changes in wind speed and direction, i.e.,
276 with high X_{CH_4} signals when the wind blows from the dairies to the instruments. Thus, the
277 EM27/SUN are clearly able to detect variability of greenhouses gases at local scales (temporal:
278 less than 5 minutes, and spatial: less than 10 km) indicating that these mobile column
279 measurements have the potential to provide estimates of local source emissions.

280 4.2) Estimation of fluxes with EM27/SUN column measurements

281 Total column measurements are directly linked to total emissions (McKain et al., 2012) and are
282 sensitive to surface fluxes (Keppel-Aleks et al., 2012). To derive the total emissions of trace gases
283 released in the atmosphere from a source region, the "mass balance" approach is often used. In
284 its simplest form, the X_{CH_4} fluxes can be written as in Equation 2, but this requires making
285 assumptions about the homogeneity of the sources and wind shear in the PBL.

$$286 F_{X_{CH_4}} = \Delta_{X_{CH_4}} \frac{V(z)}{m(\theta)} C_{air}(z) \quad (2)$$

287 where $F_{X_{CH_4}}$ is the flux (molecules/s.m²), $\Delta_{X_{CH_4}}$ is the X_{CH_4} enhancement between the upwind and
288 the downwind region (ppb), V is the average wind speed (ms⁻¹) from both airports, m is the
289 distance in meter that air crosses over the dairies calculated as a function of the wind direction
290 θ , and $SC_{air}(z)$ is the vertical column density of air (molecules/m²). The distances that airmasses
291 cross over the dairies (m) before reaching a receptor (EM27/SUN) are computed for each day,
292 each wind direction, and each instrument (see complementary information section S3).



293 Equation 2 can be reformulated as:

$$294 \quad \Delta_{X_{CH_4}} = \Delta t \cdot \frac{F_{X_{CH_4}}}{C_{air}(z)} \quad (3)$$

295 where $\Delta t = \frac{m(\theta)}{V(z)}$ is the residence time of air over the dairies (in seconds).

296 A modified version of this mass balance approach has been used by Chen et al. (2016) to verify
297 that the X_{CH_4} gradients measured by the EM27/SUN are comparable to the expected values
298 measured at Chino during the CalNex aircraft campaign (Peischl et al., 2013). In Chen et al., X_{CH_4}
299 enhancements measured between upwind and two of the downwind sites on January 24th (day
300 of constant wind direction, Figure 1 panels f and i) are compared to the expected value derived
301 from Peischl's emission numbers, which were determined using the bottom-up method and
302 aircraft measurements. They found that the measured X_{CH_4} gradient of ~ 2 ppb, agrees within the
303 low range of the 2010 value. However, this differential approach, using upwind and downwind
304 measurements, reduces the flux estimates to only one day (January 24th), since the wind speed
305 and direction were not constant during the other days of field measurements.

306 In this study, we extend the analysis of the Chino dataset using the mass balance approach on
307 steady-wind day (on January 24th) for all the FTS instruments (i.e three downwind sites), as well
308 as employing the other two days of measurements (January 15th, and 16th) in conjunction the
309 WRF-LES model to derive a flux of X_{CH_4} from the dairy farms. We exclude measurements from
310 January 22nd and August 13th because of the presence of cirrus clouds during those days, which
311 greatly reduce the precision of the column measurements. Our X_{CH_4} signal measured by the FTS
312 can be decomposed as the sum of the background concentration and the enhancements due to
313 the local sources:

$$314 \quad X_{CH_4,measured} = X_{CH_4,background} + \Delta_{X_{CH_4}} \quad (4)$$

315 Gradients of X_{CH_4} ($\Delta_{X_{CH_4}}$) are calculated relative to one instrument for the three days. The X_{CH_4}
316 means (and standard deviations) over the three days of measurements at Chino are 1.824
317 (± 0.003) ppm, 1.833 (± 0.007) ppm, 1.823 (± 0.003) ppm, and 1.835 (± 0.010) ppm for the Caltech,
318 Harvard1, Harvard2, and LANL instruments, respectively. The Harvard2 X_{CH_4} mean and standard



319 deviation are the lowest of all the observations, therefore these measurements are used to
 320 calculate gradients of X_{CH_4} for the other three instruments. Gradients of X_{CH_4} ($\Delta_{X_{CH_4}}$) for an
 321 instrument i (i.e. Caltech, Harvard1, or LANL) are the differences between each 10-minute
 322 average X_{CH_4} measured by i and the corresponding 10-minute average X_{CH_4} measured by the
 323 Harvard2 instrument. Details about the residence time calculation can be found in the
 324 supplementary information section (S3). Time series of anomalies for individual measurements
 325 days are presented in Figure 4.

326 Assuming the background levels X_{CH_4} are similar at all the instrument sites within 10 km distance
 327 and steady state wind fields, equation 3 can be written as:

$$328 \quad (X_{CH_4,i} - X_{CH_4,Harvard2}) \propto (t_i - t_{Harvard2}) \cdot F_{X_{CH_4}} \quad (5)$$

329 Graphical representation of equation 5 is shown in Figure 5 in which $\Delta_{X_{CH_4}}$, the measured
 330 gradients by the four FTS during January 24th, is plotted as a function of Δ_t , so that the slope
 331 corresponds to a flux in ppb/s or ppt/s (parts per trillion). In this figure the slope of the blue lines
 332 (dark and light ones) represents the flux measured at Chino in previous studies (Peischl et al.,
 333 2013). These studies estimating CH_4 fluxes at Chino in 2010 reported a bottom-up value of 28
 334 Gg/yr with a range of top-down measurements from 24 to 74 Gg/yr (Table 1). To compare these
 335 values (in Gg/yr) to the fluxes derived from column average (in ppt/s), we used Equation 6:

$$336 \quad F_{col} = \frac{F \cdot 10^9}{a \cdot Y \cdot C_{air}(z) \cdot \frac{m_g}{Na}} \cdot 10^{12} \quad (6)$$

337 where F_{col} is the column average flux in ppt/s, F the flux in Gg/yr, a the area of Chino (m), Y
 338 the number of seconds in a year, $C_{air}(z)$ the vertical column density of air (molecules/m²), m_g
 339 the molar mass of CH_4 (g/mol), and Na the Avogadro constant (mol⁻¹).

340 On January 24th, when the wind speed is higher than the other days (Figure 1, panels f, and i), the
 341 residence time over the dairies (Δ_t) is reduced by a factor of 30. The mean Δ_t from the closest to
 342 the furthest instruments to the upwind site are 4 minutes for Caltech (black square, Figure 5), 13
 343 minutes for Harvard2 (green square, Figure 5), and 16 minutes for LANL (red square, Figure 5).
 344 The X_{CH_4} fluxes estimated using the mean states (mass balance approach) are 4.8, 1.6, and 1.4



345 ppt/s for the Caltech, LANL, and Harvard2 downwind instruments. Overall, the FTS network infers
346 X_{CH_4} emissions at Chino that are in the low-end of previous top-down estimates reported by
347 Peischl et al. (2013), which is consistent with the decrease in cows and farms in the Chino area
348 over several past years.

349 However, the flux estimated using the closest instrument/shortest residence time (i.e. Caltech)
350 exceeds the value from previous studies by almost a factor of two. The other values from LANL
351 and Harvard2, on the other hand, are lower than previous published values. This analysis
352 demonstrates that, even with the steady-state winds day, and the simple geometry, the mass
353 balance still have weaknesses, since it does not properly explain the differences seen among the
354 three downwind sites. The close-in site exhibits the highest apparent emission rate possibly due
355 to the proximity of a large CH_4 source. This exhibits delusive approximations implied by this
356 method (i.e., spatial inhomogeneity of X_{CH_4} sources completely averaged out and conservative
357 transport in the domain) even on “golden day” of strong steady-state wind pattern. Therefore,
358 when investigating emissions at local scales these assumptions can be dubious and lead to errors
359 in the flux estimates.

360 4.3) Spatial study of the CH_4 fluxes using WRF-LES data

361 Analysis of the spatial sources at Chino is developed in this section using the WRF-LES model and
362 in section 4.4 with in situ Picarro measurements.

363 To map the sources of CH_4 at Chino with the model, we focus on the two days of measurements
364 during which the wind changed direction regularly (i.e. January 15th and 16th, Figure 1 panels d,
365 e, g and h). This provides the model information about the spatial distribution of CH_4 emissions.

366 4.3.1) WRF-LES model evaluation

367 The two WRF-Chem simulations were evaluated for both days (January 15th and 16th) using
368 meteorological observations (Figures 6 and 7). Starting with the larger region on the 3-km grid
369 where WMO sondes are available (Figure 6), model verification for both days indicates that wind
370 speed errors averaged over the domain are only about 1 ms^{-1} in the free atmosphere and slightly
371 larger in the PBL (less than 2 ms^{-1}). For wind direction, the Mean Absolute Error (MAE) is less than



372 20 degrees in the free atmosphere and increases approaching the surface, reaching a maximum
373 of about 50 degrees there. More relevant to this study, the Mean Error (ME) remains small over
374 the profile and more specifically in the PBL, oscillating between 0 and 10 degrees. At higher
375 resolutions, the comparison between observed and WRF-predicted surface wind speed (Figure
376 7) indicates that WRF is able to reproduce the overall calm wind conditions for both days at both
377 WMO stations, Chino (KCNO) and Ontario (KONT). However, measurements below 1.5 ms^{-1} are
378 not reported following the WMO standards, which limits the ability to evaluate the model over
379 time. On January 15th at KCNO, consistent with the observations, all domains except the 3-km
380 grid predict no surface wind speeds above 2 ms^{-1} from 16:00 – 19:00 UTC, except for one time
381 from the 111-m LES domain. After this period, the 111-m LES domain successfully reproduces the
382 afternoon peak in wind speed of about 3 ms^{-1} , only slightly larger than the observed values (3.6
383 ms^{-1} at Chino and 3.9 ms^{-1} at Ontario airports). However, we should not expect perfect
384 correspondence between the observations and the instantaneous LES output unless a low-pass
385 filter is performed on the LES to average out the turbulence. On January 16th 2015, the model
386 wind speed at KONT remained low throughout the day, in good agreement with the (unreported)
387 measurements, and also with available observations.

388 4.3.2) Dispersion of tracers in LES mode: 15th and 16th January 2015

389 We use the January 15th 2015 case as an example showing the detail in the local winds that can
390 be provided by the high-resolution LES domain. Prior to approximately 19:00 UTC (= 11:00 LT) a
391 brisk easterly flow is present in the valley up to a height of 2 km; however, near the surface, a
392 cold pool up to several hundred meters thick developed with only a very weak easterly motion.
393 A simulated tracer released from a location near the east edge of the Chino area stays confined
394 to the cold pool for this period (Figure 8, upper row). Solar heating causes the cold pool to break
395 down quite rapidly after 19:00 UTC, causing the low-level wind speed to become more uniform
396 with height (around 3 ms^{-1} from the east), and allowing the tracer to mix up to a height of about
397 1 km (Figure 8, middle row). Beginning around 22:00 UTC (= 14:00 LT) however, a pulse of easterly
398 flow scours out the valley from the east, while a surge of cooler westerly flow approaches at low
399 levels from the west, undercutting the easterly flow. By 00:00 UTC (=16:00 LT) the tracer seems



400 to be concentrated in the cooler air just beneath the boundary of the two opposing air streams
401 (Figure 8, lower row).

402 The tracer released (right columns in Figure 8) from an emitting $2 \times 2 \text{ km}^2$ pixel shows complex
403 vertical structures and two different regimes over the day. At 18:00 UTC, the tracer is
404 concentrated near the surface, except toward the West with a maximum at 600 m high. At 21:00
405 UTC, the tracer is well-mixed in the vertical across the entire PBL, from 0 to about $\sim 1 \text{ km}$,
406 corresponding to convective conditions of daytime. At 00:00 UTC, the stability increased again,
407 generating a low vertical plume extent with complex structures and large vertical gradients along
408 the transect. Several updrafts and downdrafts are visible at 18:00 and 00:00 UTC, indicated by
409 the shift in wind vectors and the distribution of the tracer in the vertical (Figure 8). These spatial
410 structures are unique to the LES simulation, as the PBL scheme of the mesoscale model does not
411 reproduce turbulent eddies within the PBL.

412 In the horizontal, convective rolls and large tracer gradients are present, with visible fine-scale
413 spatial structures driven by the topography (i.e. hills in the South of the domain) and turbulent
414 eddies. Figure 9 (left panel) illustrates the spatial distribution of the mean horizontal wind at the
415 surface over the 111-m simulation domain at 18:00 UTC, just prior to the scouring out of the cold
416 pool near a large Chino feedlot. It can be seen that the near-surface air that fills the triangular
417 valley in the greater Chino area is nearly stagnant, while much stronger winds appear on the
418 ridges to the south. There are some banded structures showing increased wind speed near KONT
419 to the north of the main pool of stagnant air. Figure 9 (right panel) illustrates the wind pattern
420 for the 18:00 UTC January 16th case. The same general patterns can be seen, with the main
421 apparent differences being reduced wind speed along the southern high ridges, and more
422 stagnant air in the vicinity of KONT along with elevated wind speed bands near KCNO. These
423 results emphasize how variable the wind field structures can be from point-to-point in the valley.

424 4.3.3) Bayesian inversion and error assessment

425 We present the inverse emissions from the Bayesian analytical framework in Figures 10. The
426 Bayesian analytical solution was computed for both days, assuming a flat prior emission rate of
427 $2150 \text{ mol/km}^2/\text{hour}$ corresponding to a uniform distribution of 115000 dairy cows over 64 km^2



428 emitting methane at a constant rate of 150 kg of CH₄ per year (CARB 2015), plus 18 kg annually
429 per cow from dry manure management assumed to be on-site (Peischl et al., 2013). The colored
430 areas in Figure 10 represent the ranges of solutions defined by the Simulated Annealing (SA)
431 analysis, for the two days of the campaign (in blue and green). The Bayesian averages agree well
432 with the SA estimates, with high confidence for half of the pixels (1, 2, 3, 4, 8, 13, 15, and 16),
433 and lower confidence for the other pixels. High values coincide with high confidence, which
434 confirms the fact that large signals constrain the inverse solution better. This would possibly
435 suggest that only the largest emissions could be attributed with sufficient confidence using these
436 tools.

437 The spatial distribution of the emissions is shown in Figure 13, which directly corresponds to the
438 pixel emissions presented in Figure 10. The largest sources are located in the southern part of
439 the dairy farms area, and in the northeastern corner of the domain. Additional interpretation of
440 these results is presented in the following section. The combination of the results from two dates
441 (January 15th and 16th) is necessary in order to identify the whole southern edge of the feedlots
442 as a large source. Sensitivity results are presented in the discussion and in the supplementary
443 information section (S4 and S5). Additional sensitivity tests were performed to evaluate the
444 impact of instrument errors, introducing a systematic error of 5 ppb in X_{CH₄} measured by one of
445 the EM27/SUN. The posterior emissions increased by 3-4 Gg/year for a +5ppb bias almost
446 independent of the location of the biased instrument. This represents ~10% of the total emission
447 at Chino.

448 4.4) Spatial study of the CH₄ emissions at Chino using Picarro measurements

449 During the field campaign in January 2015, in situ measurements of CH₄, CO₂, as well as δ¹³C are
450 performed simultaneously with a Picarro instrument at the same site as the LANL EM27/SUN.
451 Fossil-related CH₄ sources, such as power plants, traffic, and natural gas, emit CH₄ with an isotopic
452 depletion δ¹³C ranging from -30 to -45 ‰, whereas biogenic methane sources, such as those from
453 enteric fermentation and wet and dry manure management in dairies and feedlots emit in the
454 range of -65 to -45 ‰ (Townsend-Small et al., 2012). During the January 2015 campaign, the δ¹³C
455 at Chino ranged from -35 to -50 ‰, indicating a mixture of fossil and biogenic sources



456 respectively. Most of the air sampled included a mixture of both sources. However, the
457 measurements with the highest CH₄ concentrations had lowest δ¹³C signatures, suggesting that
458 the major CH₄ enhancements can be attributed to the dairy farms and not the surrounding urban
459 sources.

460 On January 16th and 22nd, the Picarro and the LANL EM27/SUN were installed at the southwest
461 side of the largest dairies in Chino (red pin, Figure 1b), near a wet lagoon that is used for manure
462 management (< 150 m away). For these days, the Picarro measured enhancements of CH₄ up to
463 20 ppm above background concentrations, demonstrating that the lagoon is a large source of CH₄
464 emissions in the Chino area. The location of the lagoon was identified and verified by satellite
465 imagery, visual inspection, and also with measurements from the second Picarro instrument
466 deployed in the field on January 15th, 2015. With this instrument, CH₄ spikes up to 23 ppm were
467 observed near the wet manure lagoon. The measurements from both Picarrros and the LANL
468 EM27/SUN instrument near the lagoon suggested that this is a significant local source of CH₄
469 emissions in the Chino area.

470 As opposed to column measurements, Picarro measurements are very sensitive to the dilution
471 effect of gases in the PBL. With a low boundary layer, atmospheric constituents are concentrated
472 near the surface, and the atmospheric signal detected by the in situ surface measurements is
473 enhanced relative to the daytime, when the PBL is fully developed. For this reason, additional
474 Picarro measurements were made at night on August 13th 2015, when the PBL height is minimal.
475 Between 04:00 to 07:00 (LT), we performed Picarro measurements at different locations at
476 Chino, in order to map the different sources of CH₄ and verify that the large sources observed in
477 January, such as the lagoon, are still emitting in summer. Figure 11 shows the scatter plot of one
478 minute-average anomalies of CH₄ (Δ_{CH_4}) versus CO₂ (Δ_{CO_2}), colored by the δ¹³C values,
479 measured by the Picarro on the night of August 13th 2015. During that night, the isotopic range
480 of δ¹³C in sampled methane range from -45 ‰ to -65 ‰. These low δ¹³C values are consistent
481 with the expectation that the sources of CH₄ in the Chino area are dominated by biogenic
482 emissions from dairy cows. In the feedlots (side triangles, Figure 11), Δ_{CH_4} and Δ_{CO_2} are well
483 correlated ($r^2 = 0.90$), because cows emit both gases (Kinsman et al., 1995). The observed
484 $\Delta_{CH_4}/\Delta_{CO_2}$ emission ratio, 48 ± 1.5 ppb/ppm, is in good agreement with a previous study



485 measuring this ratio from cow's breath (Lassen et al., 2012). Measurements obtained at less than
486 one meter away from cows (circles, Figure 11), had the lowest the $\delta^{13}\text{C}$ observed, $\sim -65\text{ ‰}$, and
487 these points scale well with the linear correlation observed during the survey. This confirms that
488 the emission ratio derived surveying the feedlots is representative of biogenic emissions related
489 to enteric fermentation. Measurements obtained next to the lagoon (diamond marks, Figure 11),
490 the $^{12}\text{CH}_4$ concentrations enhanced by up to 40 ppm above background levels observed that
491 night, while the relative enhancement of CO_2 was much smaller. This extremely large CH_4
492 enhancement relative to CO_2 indicates a signature of CH_4 emissions from wet manure
493 management (lagoon), confirming that there is significant heterogeneity in the CH_4 sources
494 within the Chino dairy area.

495 5) Discussion

496 The fluxes derived by the FTS observations and the WRF-LES inversions, as well as previous
497 reported values are summarized in Table 1.

498 The top-down CH₄ estimate using FTS observations in Chino provide a range of fluxes from 1.4 to
499 4.8 ppt/s during January 2015 (Table 1), which are on the lower-end than previously published
500 estimates. These values of CH₄ flux estimates for January 2015 based on the FTS measurements
501 are consistent with the decrease in cows in Chino over the past several years as urbanization
502 spreads across the region.

503 Considering the decrease of dairy cows number by ~20% from 2010 to 2015, and using the
504 emission factor of 168 kg/yr per head (CARB 2015 inventory: enteric fermentation + dry manure
505 management), the CH₄ flux associated with dairy cows at Chino decreased from 2.0 to 1.7 ppt/s,
506 which agrees well with our low flux estimates derived from FTS observations. However, fluxes
507 derived using the simple mass balance approach differs from each other, exhibiting the
508 limitations of this method, even on a “golden day” (steady-state wind day on January 24th). The
509 WRF-LES inversions (Figures 10 and 12) and mobile in situ measurements with the Picarro
510 instrument (Figure 11) indicate that the CH₄ sources are not homogeneous within this local area.
511 In addition, wind measurements from the two local airports typically disagree regarding the
512 direction and speed (Figure 1, panels d, e, f, g, h, and i), and the WRF-LES tracer results indicate
513 non-homogeneous advection of tracers (Figure 8, right panels).

514 Figure 12 shows the map of the *a posteriori* X_{CH₄} fluxes (mean of January 15th and 16th runs) from
515 the WRF-LES simulations, superimposed on a Google earth map, with the location of dairy farms
516 represented by the red areas. The domain is decomposed into 16 boxes (Section 3.2), in which
517 the colors correspond to the *a posteriori* emissions derived from the WRF-LES inversions. Red
518 (blue) colors of a box mean more (less) CH₄ emissions compared to the *a priori* emissions, which
519 corresponds to the dairy cow emissions contained in the CARB 2015 inventory (emission factor
520 multiplied by the number of cows). Results of the inversion exhibit more CH₄ emissions at the
521 South and the Northeast parts of the domain, and emissions corresponding to dairy cows in the
522 center of the area.



523 The higher CH₄ emissions from the southwestern part of the domain can be attributed to the wet
524 manure lagoon (yellow pin, Figure 12) in January 2015. During the night of August 13th 2015,
525 Picarro measurements confirmed that the lagoon was still wet and emitted a considerable
526 amount of CH₄ relative to CO₂ (Figure 12). The second mobile Picarro instrument from JPL was
527 deployed on January 15th 2015 and measured CH₄ spikes up to 23 ppm near the wet manure
528 lagoon. The WRF-LES model also suggests higher methane fluxes in these regions (red boxes,
529 Figure 12). The CARB 2015 inventory estimates that manure management practices under wet
530 (e.g. lagoon) conditions emit more CH₄ than the dairy cows themselves: 187 kg CH₄ cow⁻¹ yr⁻¹
531 from wet manure management, 18 kg CH₄ cow⁻¹ yr⁻¹ from dry management practices, and 150 kg
532 CH₄ cow⁻¹ yr⁻¹ from enteric fermentation in the stomachs of dairy cows. Therefore, we expect
533 measurements in which the lagoon emissions were detected by our instruments will lead to
534 higher methane fluxes in the local region, compared to measurements detecting emissions from
535 enteric fermentation in cows alone. Bottom-up emission inventory of CH₄ is 2 times higher when
536 considering wet lagoons (Wennberg et al., 2012) instead of dry management practices (Peischl
537 et al., 2013) at Chino (Table1). The location and extent of wet lagoons in the Chino region is not
538 expected to be constant with time and could be altered due to changing land use and future
539 development in the area. Bottom-up estimates of CH₄ emissions from dairies in the Chino region
540 could be further improved if the extent and location of wet manure lagoons were well-known.

541 The WRF-LES model also suggests higher methane fluxes in the Southeast (red boxes, Figure 13).
542 No dairy farms are located in these areas, but an inter-state pipelines is located nearby, thus
543 these CH₄ enhancements could be attributed to natural gas. The ¹³CH₄ Picarro measurements
544 indicate the Chino area is influenced by both fossil- and biogenic- related methane sources. A
545 recent study has suggested the presence of considerable fugitive emissions of methane at Chino
546 (<http://www.edf.org/climate/methanemaps/city-snapshots/los-angeles-area>), probably due to
547 the advanced age of the pipelines. Natural gas leaks in the Chino area were not specifically
548 targeted during the time of this field campaign and cannot be confirmed using available data.
549 This possibility should thus be confirmed by future studies.

550 In addition to possible fugitive emissions at Chino, the inversion also predicts higher CH₄ flux in
551 the Northeastern region of the study domain, which is in the vicinity of a power plant that



552 reportedly emits a CH₄ flux roughly equivalent of one cow per year (only including enteric
553 fermentation) (http://www.arb.ca.gov/cc/reporting/ghg-rep/reported_data/ghg-reports.htm).
554 Further analysis and measurements of fossil methane sources in the Chino area would help verify
555 potential contributions from fossil methane sources, including power plants and/or fugitive
556 natural gas pipeline emissions.

557 Overall, FTS and in situ Picarro measurements, as well as WRF-LES inversions, all demonstrate
558 that the CH₄ sources at Chino are heterogeneous, with a mixture of emissions from enteric
559 fermentation, wet and dry manure management practices, and possible additional fossil
560 methane emissions (from natural gas pipeline and power plants). The detection of CH₄ emissions
561 in the Chino region and discrepancies between top-down estimates could be further improved
562 with more FTS observations and concurrent in situ methane isotopes measurements combined
563 with high-resolution WRF-LES inversions. This would improve the spatial detection of the CH₄
564 emissions at Chino, in order to ameliorate the inventories among the individual sources in this
565 local area.

566 6) Summary and conclusions

567 In January 2015, four mobile low-resolution FTS (EM27/SUN) were deployed in a ~6 x 9 km area
568 in Chino (California), to assess CH₄ emissions related to dairy cows in the SoCAB farms. The
569 network of column measurements captured large spatial and temporal gradients of greenhouses
570 gases emitted from this small-scale area. Temporal variabilities of X_{CH₄} and X_{CO₂} can reach up to
571 20 ppb and 2 ppm, respectively, within less than a 10-minute interval with respect to wind
572 direction changes. This study demonstrate that these mobile FTS are therefore capable of
573 detecting local greenhouses gas signals and these measurements can be used to improve the
574 verification of X_{CO₂} and X_{CH₄} emissions at local scales.

575 Top-down estimates of CH₄ fluxes using the 2015 FTS observations in conjunction with wind
576 measurements are 1.4-4.8 ppt/s, which are in the low-end of the 2010 estimates (Peischl et al.,
577 2013), consistent with the decrease in cows in the Chino area. During this campaign, FTS
578 measurements were collected in close proximity to the sources (less than a few km) in order to
579 capture large signals from the local area. The main advantage of this type of deployment strategy
580 is to better constrain the emissions, while avoiding vertical mixing issues in the model with the
581 use of column measurements in the inversion. Therefore, the model transport errors, which
582 often limit the capacity of the model flux estimates, are considerably reduced. However, the close
583 proximity of the measurements to the sources makes the assumptions about homogeneity of the
584 sources and wind patterns questionable.

585 The FTS and the Picarro measurements detected various CH₄ signatures over Chino, with extreme
586 CH₄ enhancements measured nearby a wet lagoon (Picarro and FTS measurements enhanced by
587 40 ppm CH₄ and 60 ppb X_{CH₄}, respectively) and possible fugitive fossil-related CH₄ emissions in
588 the area (indicated by higher δ¹³C values than expected from biogenic emissions alone).

589 Wind speed and direction measurements derived from the two local airports (less than 10 km
590 apart), as well as the WRF meteorological simulations at different FTS sites, differ greatly with
591 each other, suggesting that an assumption of steady horizontal wind incorrect in the use of the
592 mass balance approach in our study. This may explain some discrepancy between the CH₄ flux
593 estimates from the mass balance approach and the Bayesian inversion.



594 This study demonstrates the value of using mobile column measurements for detection of local
595 CH₄ enhancements and the estimation of CH₄ emissions when these measurements are
596 combined with high-resolution modeling. High-resolution WRF-LES simulations were performed
597 on two dates, constrained by four column measurements each day, to map the heterogeneous
598 CH₄ sources at Chino. The average a posteriori flux over the domain is 3.2 ppt/s when only
599 considering the boxes in the center of the domain, and 4.7 ppt/s when all the boxes are averaged.
600 The major emitter (a wet manure lagoon) was identified by the inversion results, and is supported
601 by in-situ ¹³CH₄ measurements collected during the campaign. The CH₄ flux estimates are within
602 the range of the top-down mass balance emissions derived with the four FTS and estimates
603 reported by Peischl et al. 2013 (i.e., 2.1 to 6.5 ppt/s), showing that column measurements
604 combined with high resolution modeling can detect and possibly estimate CH₄ emissions.

605 The instrumental synergy (mobile in situ and column observations) coupled with a
606 comprehensive high-resolution model simulations allow estimation of local CH₄ fluxes, and can
607 be useful for improving emission inventories, especially in a complex megacity area, where the
608 different sources are often located within small areas.

609 This study highlights the complexity of estimating emissions at local scale when sources and wind
610 can exhibit heterogeneous patterns. Long term column observations and/or aircraft eddy
611 covariance measurements could improve estimations.

612 Acknowledgements:

613 The authors thank NASA and the W. M. Keck Institute for Space Studies for financial support.
614 MKD acknowledges NASA CMS support of the EM27/SUN deployment and LANL- LDRD
615 20110081DR for acquisition of the instrument. J. Chen, T. Jones, J. E. Franklin, and S. C. Wofsy
616 gratefully acknowledge funding provided by the National Science Foundation through MRI Award
617 1337512. January Campaign participants are Camille Viatte, Jacob Hedelius, Harrison Parker, Jia
618 Chen, Johnathan Franklin, Taylor Jones, Riley Duren, and Kristal Verhulst.



619

References:

620 Air Resources Board (ARB): concept paper, full report, May 7th 2015, available at:
621 http://www.arb.ca.gov/cc/shortlived/concept_paper.pdf, 2015.

622 Arata, C., Rahn, T., and Dubey, M. K.: Methane Isotope Instrument Validation and Source
623 Identification at Four Corners, New Mexico, United States, *J. Phys. Chem. A*, doi:
624 10.1021/acs.jpca.5b12737, 2016.

625 Berchet, A., Pison, I., Chevallier, F., Paris, J.-D., Bousquet, P., Bonne, J.-L., Arshinov, M. Y., Belan,
626 B. D., Cressot, C., Davydov, D. K., Dlugokencky, E. J., Fofonov, A. V., Galanin, A., Lavrič, J., Machida,
627 T., Parker, R., Sasakawa, M., Spahni, R., Stocker, B. D., and Winderlich, J.: Natural and
628 anthropogenic methane fluxes in Eurasia: a mesoscale quantification by generalized atmospheric
629 inversion, *Biogeosciences*, 12, 5393-5414, doi:10.5194/bg-12-5393-2015, 2015.

630 Breon, F. M. and Ciais, P.: Spaceborne remote sensing of greenhouse gas concentrations,
631 *Comptes Rendus Geoscience*, 342, 412–424, doi: 10.1016/j.crte.2009.09.012, 2010.

632 California Agricultural Statistics, United States Department of Agriculture, National Agricultural
633 Statistics Service, Pacific Regional, Field Office California, full report, available at:
634 [http://www.nass.usda.gov/Statistics_by_State/California/Publications/California_Ag_Statistics/](http://www.nass.usda.gov/Statistics_by_State/California/Publications/California_Ag_Statistics/CALivestockandDairy.pdf)
635 [CALivestockandDairy.pdf](http://www.nass.usda.gov/Statistics_by_State/California/Publications/California_Ag_Statistics/CALivestockandDairy.pdf), 2013.

636 California Air Resources Board (CARB): California Greenhouse Gas Emission Inventory - 2015
637 Edition, available from: <http://www.arb.ca.gov/cc/inventory/data/data.htm>, 2015.

638 Cambaliza, M. O. L., Shepson, P. B., Caulton, D. R., Stirm, B., Samarov, D., Gurney, K. R., Turnbull,
639 J., Davis, K. J., Possolo, A., Karion, A., Sweeney, C., Moser, B., Hendricks, A., Lauvaux, T., Mays, K.,
640 Whetstone, J., Huang, J., Razlivanov, I., Miles, N. L., and Richardson, S. J.: Assessment of
641 uncertainties of an aircraft-based mass balance approach for quantifying urban greenhouse gas
642 emissions, *Atmos. Chem. Phys.*, 14, 9029–9050, doi:10.5194/acp-14-9029-2014, 2014.

643 Chen, J., Viatte, C., Hedelius, J. K., Jones, T., Franklin, J. E., Parker, H., Gottlieb, E. W., Wennberg,
644 P. O., Dubey, M. K., and Wofsy, S. C.: Differential Column Measurements Using Compact Solar-



645 Tracking Spectrometers, Atmos. Chem. Phys. Discuss., doi:10.5194/acp-2015-1058, in review,
646 2016.

647 Ciais, P., Sabine, C., Bala, G., Bopp, L., Brovkin, V., Canadell, J., Chhabra A., DeFries, R., Galloway,
648 J., Heimann, M., Jones, C., Le Quéré, C., Myneni, R.B., Piao, S., and Thornton, P.: Carbon and Other
649 Biogeochemical Cycles. In: Climate Change 2013: The Physical Science Basis. Contribution of
650 Working Group I to the Fifth Assessment Report of the Intergovernmental Panel on Climate
651 Change [Stocker, T.F., Qin, D., Plattner, G.-K., Tignor, M., Allen, S.K., Boschung, J., Nauels, A., Xia,
652 Y., Bex, V. and Midgley, P.M. (eds.)]. Cambridge University Press, Cambridge, United Kingdom
653 and New York, NY, USA, 2013.

654 Deng, A., Stauffer, D., Gaudet, B., Dudhia, J., Hacker, J., Bruyere, C., Wu, W., Vandenberghe, F.,
655 Liu, Y., and Bourgeois, A.: Update on WRF-ARW end-to-end multi-scale FDDA system. 10th Annual
656 WRF Users' Workshop, Boulder, CO, 23 Jun 2009.

657 Environmental Protection Agency (EPA): Sources of Greenhouses Gases Emissions: addresses
658 anthropogenic emissions from agricultural activities (not including fuel combustion and sewage
659 emissions, which are addressed in the Energy and Waste chapters), full report, available from:
660 [http://www.epa.gov/climatechange/Downloads/ghgemissions/US-GHG-Inventory-2015-](http://www.epa.gov/climatechange/Downloads/ghgemissions/US-GHG-Inventory-2015-Chapter-5-Agriculture.pdf)
661 [Chapter-5-Agriculture.pdf](http://www.epa.gov/climatechange/Downloads/ghgemissions/US-GHG-Inventory-2015-Chapter-5-Agriculture.pdf), 2015.

662 Forster, P., Ramaswamy, V., Artaxo, P., Berntsen, T., Betts, R., Fahey, D.W., Haywood, J., Lean, J.,
663 Lowe, D.C., Myhre, G., Nganga, J., Prinn, R., Raga, G. M. S., Van Dorland, R.: Changes in
664 Atmospheric Constituents and in Radiative Forcing. In: S. Solomon et al. (Editors), Climate Change
665 2007: The Physical Science Basis. Contribution of Working Group I to the Fourth Assessment
666 Report of the Intergovernmental Panel on Climate Change. Cambridge University Press,
667 Cambridge, U.K, doi:10.1017/CBO9781107415324, 2007.

668 Franco, B., Hendrick, F., Van Roozendaal, M., Müller, J.-F., Stavrakou, T., Marais, E. A., Bovy, B.,
669 Bader, W., Fayt, C., Hermans, C., Lejeune, B., Pinardi, G., Servais, C., and Mahieu, E.: Retrievals of
670 formaldehyde from ground-based FTIR and MAX-DOAS observations at the Jungfraujoch station
671 and comparisons with GEOS-Chem and IMAGES model simulations, Atmos. Meas. Tech., 8, 1733-
672 1756, doi:10.5194/amt-8-1733-2015, 2015.



- 673 Gisi, M., Hase, F., Dohe, S., and Blumenstock, T.: Camtracker: a new camera controlled
674 high precision solar tracker system for FTIR-spectrometers, *Atmos. Meas. Tech.*, 4, 47–54,
675 doi:10.5194/amt-4-47-2011, 2011.
- 676 Gisi, M., Hase, F., Dohe, S., Blumenstock, T., Simon, A., and Keens, A.: XCO₂-measurements with
677 a tabletop FTS using solar absorption spectroscopy, *Atmos. Meas. Tech.*, 5, 2969–2980,
678 doi:10.5194/amt-5-2969-2012, 2012.
- 679 Gordon, M., Li, S.-M., Staebler, R., Darlington, A., Hayden, K., O'Brien, J., and Wolde, M.:
680 Determining air pollutant emission rates based on mass balance using airborne measurement
681 data over the Alberta oil sands operations, *Atmos. Meas. Tech.*, 8, 3745–3765, doi:10.5194/amt-
682 8-3745-2015, 2015.
- 683 Grell, G.A., Peckham, S.E., Schmitz, R., McKeen, S.A., Frost, G., Skamarock, W.C., and Eder, B.:
684 Fully coupled online chemistry within the WRF model, *Atmos. Environ.*, 39, 6957–6975, 2005.
- 685 Guha, A., Gentner, D. R., Weber, R. J., Provencal, R., and Goldstein, A. H.: Source apportionment
686 of methane and nitrous oxide in California's San Joaquin Valley at CalNex 2010 via positive matrix
687 factorization, *Atmos. Chem. Phys. Discuss.*, 15, 6077–6124, doi:10.5194/acpd-15-6077-2015,
688 2015.
- 689 Hase, F., Frey, M., Blumenstock, T., Groß, J., Kiel, M., Kohlhepp, R., Mengistu Tsidu, G.,
690 Schäfer, K., Sha, M. K., and Orphal, J.: Use of portable FTIR spectrometers for detecting
691 greenhouse gas emissions of the megacity Berlin – Part 2: Observed time series of XCO₂ and XCH₄,
692 *Atmos. Meas. Tech. Discuss.*, 8, 2767–2791, doi:10.5194/amtd-8-2767-2015, 2015.
- 693 Hedelius J. K., Viatte, C., Wunch, D., Roehl, C., Toon, G. C., Chen, J., Jones, T., Wofsy, S. C., Franklin,
694 J. E., Parker, H., Dubey, M., and Wennberg, P. O.: Assessment of errors and biases in Xgas
695 retrieved from a low resolution spectrometer (EM27/SUN), in preparation to be submitted in
696 AMT, 2016.
- 697 Hiller, R. V., Neininger, B., Brunner, D., Gerbig, C., Bretscher, D., Künzle, T., Buchmann, N., and
698 Eugster, W.: Aircraft-based CH₄ flux estimates for validation of emissions from an agriculturally
699 dominated area in Switzerland, *J. Geophys. Res. Atmos.*, 119, doi:10.1002/2013JD020918, 2014.



- 700 Histov, A. N., Johnson, K. A., and Kebreab, E.: Livestock methane emissions in the United States,
701 P. Natl. Acad. Sci., 111 (14), E1320, doi: 10.1073/pnas.1401046111, 2014.
- 702 Hsu, Y.-K., VanCuren, T., Park, S., Jakober, C., Herner, J., FitzGibbon, M., Blake, D. R., and Parrish,
703 D. D.: Methane emissions inventory verification in southern California, Atmos. Environ., 44, 1–7,
704 doi:10.1016/j.atmosenv.2009.10.002, 2010.
- 705 Intergovernmental Panel on Climate Change (IPCC): Climate Change 2013: the physical science
706 basis. Contribution of working group I to the fifth Assessment report of the Intergovernmental
707 Panel On Climate Change [Stocker, T.F., Qin, D., Plattner, G.-K., Tignor, M., Allen, S.K., Boschung,
708 J., Nauels, A., Xia, Y., Bex, V. and Midgley, P.M. (eds.)]. Cambridge University Press, Cambridge,
709 United Kingdom and New York, NY, USA, 1535pp, 2013.
- 710 Karion, A., Sweeney, C., Pétron, G., Frost, G., Michael Hardesty, R., Kofler, J., Miller, B. R.,
711 Newberger, T., Wolter, S., Banta, R., Brewer, A., Dlugokencky, E., Lang, P., Montzka, S. A., Schnell,
712 R., Tans, P., Trainer, M., Zamora, R., and Conley, S.: Methane emissions estimate from airborne
713 measurements over a western United States natural gas field, Geophys. Res. Lett., 40, 4393–
714 4397, doi: 10.1002/grl.50811, 2013.
- 715 Keppel-Aleks, G., Wennberg, P.O., Washenfelder, R.A., Wunch, D., Schneider, T., Toon, G.C.,
716 Andres, R.J., Blavier, J.-F., Connor, B., Davis, K.J., Desai, A.R., Messerschmidt, J., Notholt, J., Roehl,
717 C.M., Sherlock, V., Stephens, B.B., Vay, S.A., and Wofsy, S.C.: The imprint of surface fluxes and
718 transport on variations in total column carbon dioxide, Biogeosciences, 9, 875–891,
719 doi:10.5194/bg-9-875-2012, 2012.
- 720 Kinsman, R., Sauer, F.D., Jackson, H.A., Wolynetz, M.S.: Methane and Carbon Dioxide Emissions
721 from Dairy Cows in Full Lactation Monitored over a Six-Month Period, J. of Dairy Science, 78 (12),
722 2760–2766, doi:10.3168/jds.S0022-0302(95)76907-7, 1995.
- 723 Kort, E. A., Frankenberg, C., Costigan, K. R., Lindenmaier, R., Dubey, M. K., and Wunch, D.: Four
724 corners: The largest US methane anomaly viewed from space, Geophys. Res. Lett., 41, 6898–
725 6903, doi:10.1002/2014GL061503, 2014.



- 726 Lassen, J., Lovendahl, P., and Madsen, J.: Accuracy of noninvasive breath methane measurements
727 using Fourier transform infrared methods on individual cows, *J Dairy Sci.*, 95(2), 890–898, doi:
728 10.3168/jds.2011-4544, 2012.
- 729 Lauvaux, T., Schuh, A., Bocquet, M., Wu, L., Richardson, S., Miles, N., & Davis, K.: Network design
730 for mesoscale inversions of CO₂ sources and sinks. *Tellus B*, 64. doi:10.3402/tellusb.v64i0.17980,
731 2012.
- 732 Lavoie, T. N., Shepson, P. B., Cambaliza, M. O. L., Stirm, B. H., Karion, A., Sweeney, C., Yacovitch,
733 T. I., Herndon, S. C., Lan, X., and Lyon, D.: Aircraft-Based Measurements of Point Source Methane
734 Emissions in the Barnett Shale Basin, *Environ. Sci. Technol.*, 49 (13), 7904–7913, doi:
735 10.1021/acs.est.5b00410, 2015.
- 736 Leifer, I., Culling, D., Schneising, O., Farrell, P., Buchwitz, M., and Burrows, J. P.: Transcontinental
737 methane measurements: Part 2. Mobile surface investigation of fossil fuel industrial fugitive
738 emissions, *Atmos. Env.*, 74, 432–441, <http://dx.doi.org/10.1016/j.atmosenv.2013.03.018>, 2013.
- 739 Lindenmaier, R., Dubey, M. K., Henderson, B. G., Butterfield, Z. T., Herman, J. R., Rahn, T., Lee, S.-
740 H.: Multiscale observations of CO₂, 13CO₂, and pollutants at Four Corners for emission
741 verification and attribution, *Proc. Natl. Acad. Sci. U. S. A.*, 111, 8386–8391, 2014.
- 742 McKain, K., Wofsy, S. C., Nehrkorn, T., Eluszkiewicz, J., Ehleringer, J. R., and Stephens, B. B.:
743 Assessment of ground-based atmospheric observations for verification of greenhouse gas
744 emissions from an urban region, *P. Natl. Acad. Sci. USA*, 109, 8423–8428,
745 doi:10.1073/pnas.1116645109, 2012.
- 746 Miller, S. M., Wofsy, S. C., Michalak, A. M., Kort, E. A., Andrews, A. E., Biraud, S. C., Dlugokencky,
747 E. J., Eluszkiewicz, J., Fischer, M. L., Janssens-Maenhout, G., Miller, B. R., Miller, J. B., Montzka, S.
748 A., Nehrkorn, T., and Sweeney, C.: Anthropogenic emissions of methane in the United States, *P.*
749 *Natl. Acad. Sci.*, 110 (50), 20018–20022, doi: 10.1073/pnas.131439110, 2013.
- 750 Moeng, C.-H., Dudhia, J., Klemp, J., and Sullivan, P.: Examining two-way grid nesting for large eddy
751 simulation of the PBL using the WRF model, *Mon. Wea. Rev.*, 135, 2295–2311,
752 doi:10.1175/MWR3406.1, 2007.



- 753 Myhre, G., Shindell, D., Bréon, F.-M., Collins, W., Fuglestedt, J., Huang, J., Koch, D., Lamarque,
754 J.-F., Lee, D., Mendoza, B., Nakajima, T., Robock, A., Stephens, G., Takemura, T., and Zhang, H.:
755 Anthropogenic and Natural Radiative Forcing. In: Climate Change 2013: The Physical Science
756 Basis. Contribution of Working Group I to the Fifth Assessment Report of the Intergovernmental
757 Panel on Climate Change [Stocker, T.F., Qin, D., Plattner, G.-K., Tignor, M., Allen, S.K., Boschung,
758 J., Nauels, A., Xia, Y., Bex, V. and Midgley, P.M. (eds.)]. Cambridge University Press, Cambridge,
759 United Kingdom and New York, NY, USA, 2013.
- 760 Nisbet, E., and Weiss, R.: Top-down versus bottom-up, *Science*, 328 (5983), 1241–1243,
761 doi:10.1126/science.1189936, 2010.
- 762 Nowak, J. B., Neuman, J. A., Bahreini, R., Middlebrook, A. M., Holloway, J. S. S., McKeen, S. A.,
763 Parrish, D. D. D., Ryerson, T. B. B., Trainer, M. K.: Ammonia sources in the California South Coast
764 Air Basin and their impact on ammonium nitrate formation, *Geophys. Res. Lett.*, 39, L07804,
765 doi:10.1029/2012GL051197, 2012.
- 766 Peischl, J., Ryerson, T. B., Brioude, J., Aikin, K. C., Andrews, A. E., Atlas, E., Blake, D., Daube,
767 B. C., de Gouw, J. A., Dlugokencky, E., Frost, G. J., Gentner, D. R., Gilman, J. B., Goldstein, A. H.,
768 Harley, R. A., Holloway, J. S., Kofler, J., Kuster, W. C., Lang, P. M., Novelli, P. C., Santoni, G. W.,
769 Trainer, M., Wofsy, S. C., and Parrish, D. D.: Quantifying sources of methane using light alkanes
770 in the Los Angeles basin, California, *J. Geophys. Res. Atmos.*, 118(10), 4974–4990,
771 doi:10.1002/jgrd.50413, 2013.
- 772 Rogers, R. E., Deng, A., Stauffer, D. R., Gaudet, B. J., Jia, Y., Soong, S., Tanrikulu, S.: Application of
773 the Weather Research and Forecasting Model for Air Quality Modeling in the San Francisco Bay
774 Area. *J. Appl. Meteor.*, 52, 1953-1973, 2013.
- 775 Skamarock, W. C., J. B. Klemp, J. Dudhia, D. O. Gill, D. M. Barker, M. G. Duda, X.-Y. Huang, W.
776 Wang, and J. G. Powers, 2008: A description of the Advanced Research WRF version 3. NCAR
777 Technical Note 475, http://www.mmm.ucar.edu/wrf/users/docs/arw_v3.pdf.
- 778 Streets, D.G., Canty, T., Carmichael, G.R., de Foy, B., Dickerson, R.R., Duncan, B.N., Edwards, D.P.,
779 Haynes, J.A., Henze, D.K., Houyoux, M.R., Jacob, D.J., Krotkov, N.A., Lamsal, L.N., Liu, Y., Lu, Z.,



- 780 Martin, R.V., Pfister, G.G., Pinder, R.W., Salawitch, R.J., Wecht, K.J.: Emissions estimation from
781 satellite retrievals: a review of current capability, *Atmos. Environ.*, **77**, 1011–1042
782 <http://dx.doi.org/10.1016/j.atmosenv.2013.05.051>, 2013.
- 783 Stremme, W., Grutter, M., Rivera, C., Bezanilla, A., Garcia, A. R., Ortega, I., George, M., Clerbaux,
784 C., Coheur, P.-F., Hurtmans, D., Hannigan, J. W., and Coffey, M. T.: Top-down estimation of carbon
785 monoxide emissions from the Mexico Megacity based on FTIR measurements from ground and
786 space, *Atmos. Chem. Phys.*, **13**, 1357–1376, doi:10.5194/acp-13-1357-2013, 2013.
- 787 Tilman, D. and Clark, M.: Global diets link environmental sustainability and human health, *Nature*,
788 **515**, 518–522, doi:10.1038/nature13959, 2014.
- 789 Townsend-Small, A., Tyler, S.C., Pataki, D. E., Xu, X., and Christensen, L. E.: Isotopic measurements
790 of atmospheric methane in Los Angeles, California, USA reveal the influence of “fugitive” fossil
791 fuel emissions, *J. Geophysical Research*, **117**, D7, doi:10.1029/2011JD016826, 2012.
- 792 US Climate Action Plan, strategy to reduce methane, full report,
793 [https://www.whitehouse.gov/sites/default/files/strategy_to_reduce_methane_emissions_201](https://www.whitehouse.gov/sites/default/files/strategy_to_reduce_methane_emissions_2014-03-28_final.pdf)
794 [4-03-28_final.pdf](https://www.whitehouse.gov/sites/default/files/strategy_to_reduce_methane_emissions_2014-03-28_final.pdf), March 2014.
- 795 Turner, A. J., Jacob, D. J., Wecht, K. J., Maasackers, J. D., Lundgren, E., Andrews, A. E., Biraud, S.
796 C., Boesch, H., Bowman, K. W., Deutscher, N. M., Dubey, M. K., Griffith, D. W. T., Hase, F., Kuze,
797 A., Notholt, J., Ohyama, H., Parker, R., Payne, V. H., Sussmann, R., Sweeney, C., Velazco, V. A.,
798 Warneke, T., Wennberg, P. O., and Wunch, D.: Estimating global and North American methane
799 emissions with high spatial resolution using GOSAT satellite data, *Atmos. Chem. Phys.*, **15**, 7049–
800 7069, doi:10.5194/acp-15-7049-2015, 2015.
- 801 Wennberg, P. O., Mui, W., Wunch, D., Kort, E. A., Blake, D. R. Atlas, E. L., Santoni, G. W., Wofsy,
802 S. C., Diskin, G. S., Joeng, S., and Fischer, M. L.: On the sources of methane to the Los Angeles
803 atmosphere, *Environ. Sci. Technol.*, **46** (17), 9282–9289, doi:10.1021/es301138y, 2012.
- 804 Wong, K. W., Fu, D., Pongetti, T. J., Newman, S., Kort, E. A., Duren, R., Hsu, Y.-K., Miller, C. E.,
805 Yung, Y. L., and Sander, S. P.: Mapping CH₄ : CO₂ ratios in Los Angeles with CLARS-FTS from Mount
806 Wilson, California, *Atmos. Chem. Phys.*, **15**, 241–252, doi:10.5194/acp-15-241-2015, 2015.



807 Wunch, D., Wennberg, P. O., Toon, G. C., Keppel-Aleks, G., and Yavin, Y. G.: Emissions of
808 greenhouse gases from a North American megacity, *Geophys. Res. Lett.*, 36, L15810,
809 doi:10.1029/2009GL039825, 2009.

810 Wunch, D., Toon, G. C., Blavier, J.-F. L., Washenfelder, R. A., Notholt, J., Connor, B. J., Griffith, D.
811 W. T., Sherlock, V., and Wennberg, P. O.: The total carbon column observing network,
812 *Philosophical Transactions of the Royal Society - Series A: Mathematical, Physical and Engineering*
813 *Sciences*, 369(1943), 2087-2112, doi:10.1098/rsta.2010.0240, 2011.

814 Wunch, D., Toon, G. C., Sherlock, V., Deutscher, N. M., Liu, C., Feist, D. G. and Wennberg, P. O.:
815 The Total Carbon Column Observing Network's GGG2014 Data Version, 43,
816 doi:10.14291/tccon.ggg2014.documentation.R0/1221662, 2015.

817 York, D., Evensen, N. M., Lopez Martinez, M., and De Basabe Delgado, J.: Unified equations for
818 the slope, intercept, and standard errors of the best straight line, *Am J. Phys.*, 72(3), 367–375,
819 <http://dx.doi.org/10.1119/1.1632486>, 2004.

820 Zhao, C., Andrews, A. E., Bianco, L., Eluszkiewicz, J., Hirsch, A., MacDonald, C., Nehr Korn, T., and
821 Fischer, M. L.: Atmospheric inverse estimates of methane emissions from Central California, *J.*
822 *Geophys. Res.*, 114, D16302, doi:10.1029/2008JD011671, 2009.

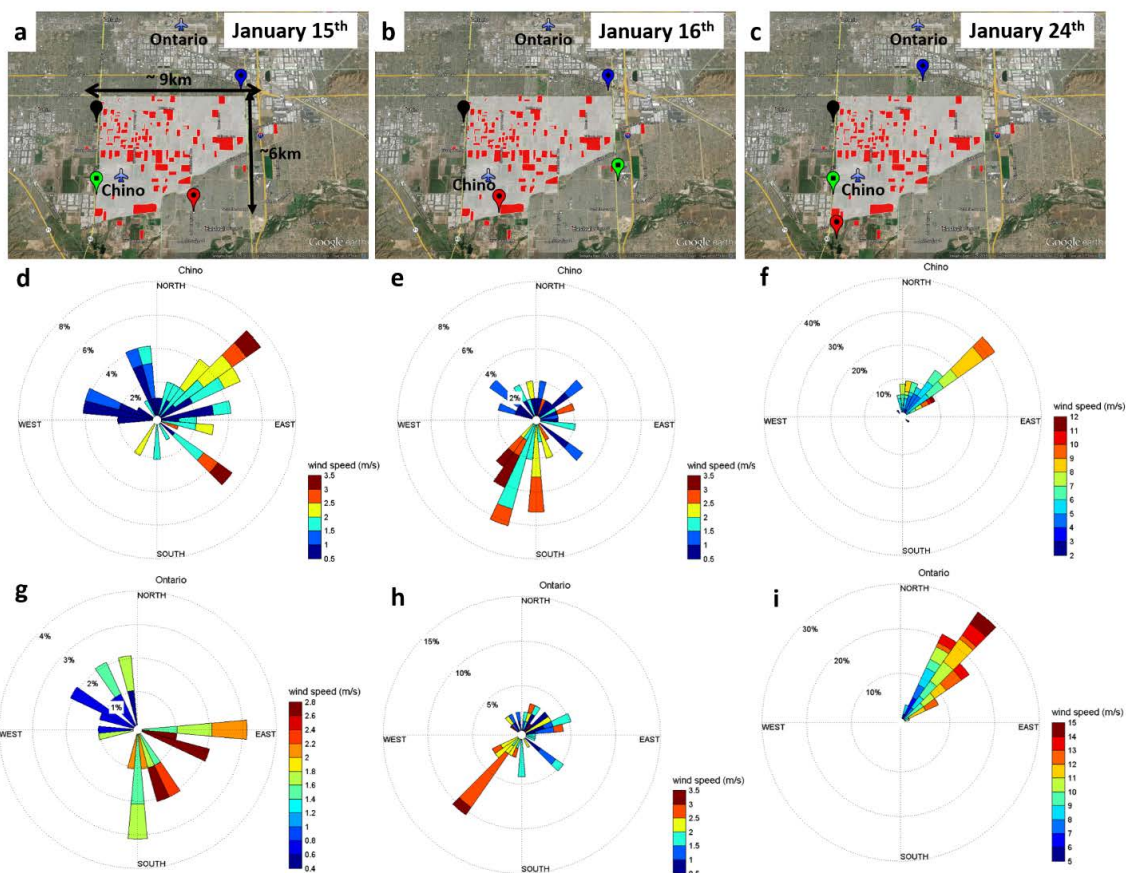


study	time of study	sources	CH ₄ emission (Gg/year)	CH ₄ emission (ppt/s)
Peischl et al., 2013	2010	inventory (dry manure + cows)	28	2.5
Peischl et al., 2013	2010	aircraft measurements	24-74	2.1-6.5
Wennberg et al., 2012	2010	inventory (wet manure + cows)*	66	5.8
CARB 2015	2015	inventory (dry manure + cows)	19	1.7
This study	2015	FTS measurements only	16-55	1.4-4.8
This study	2015	WRF inversions	36-54	3.2-4.7

823

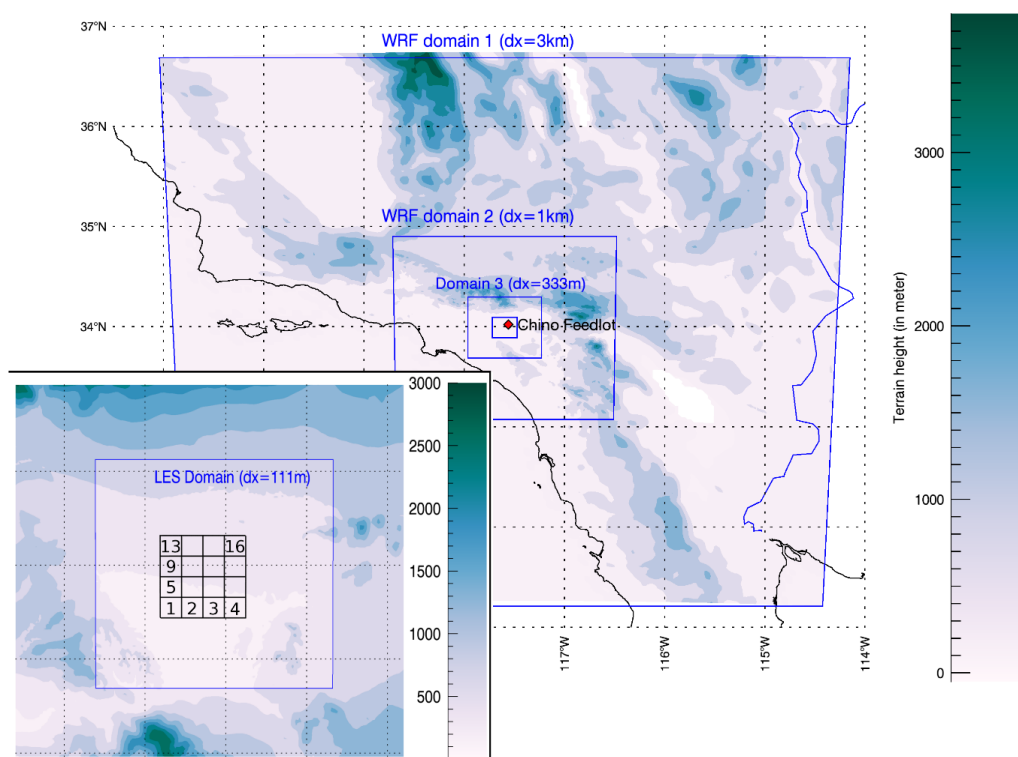
824 * Value reported for the SoCAB, apportioned for Chino in this study.

825 Table1: Emissions of CH₄ at Chino.



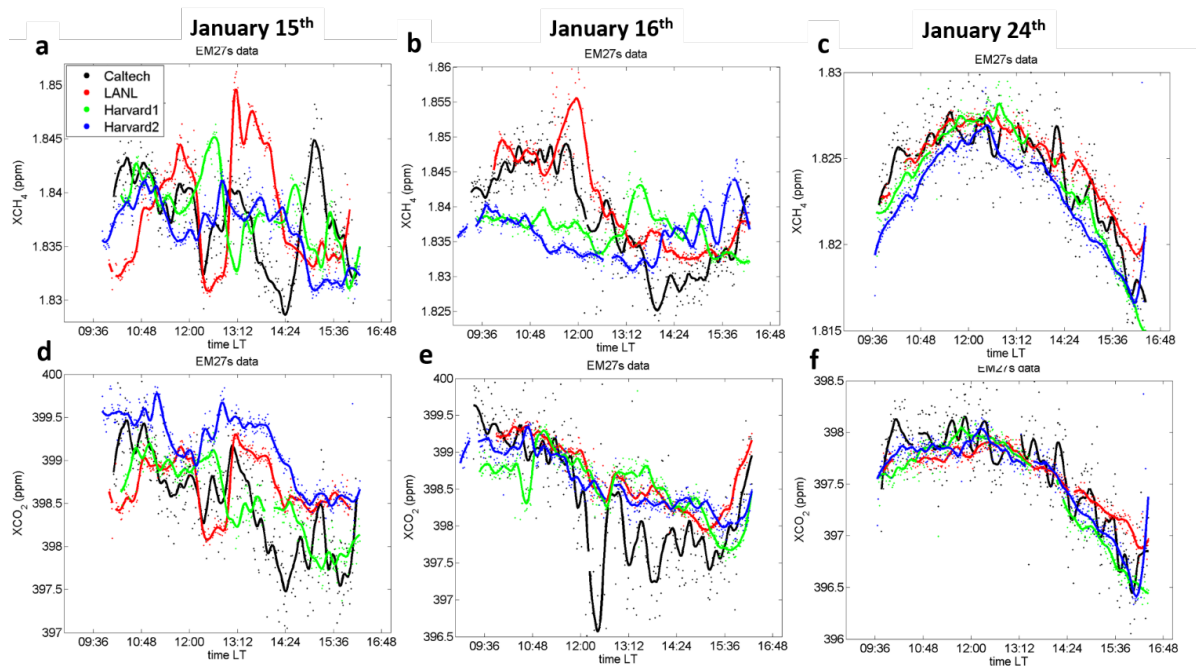
826

827 Figure 1: Three different days of measurements during the field campaign at Chino (~9 x 6 km) on the 15th,
828 16th, and 24th of January 2015. Upper panels (a, b, and c) show the chosen locations of the four EM27/SUN
829 (black, red, green, and blue pins correspond to the Caltech, LANL, Harvard1, and Harvard2 instruments,
830 respectively). The red marks on the map correspond to the dairy farms. Lower panels show wind roses of
831 ten-minute average of wind directions and wind speeds measured at the two local airports (at Chino on
832 panels d, e, and f, and at Ontario on panels g, h, and i). Map provided by GOOGLE EARTH V 7.1.2.2041, US
833 Dept. of State Geographer, Google, 2013, Image Landsat, Data SIO, NOAA, U.S. Navy, NGA, and GEBCO.



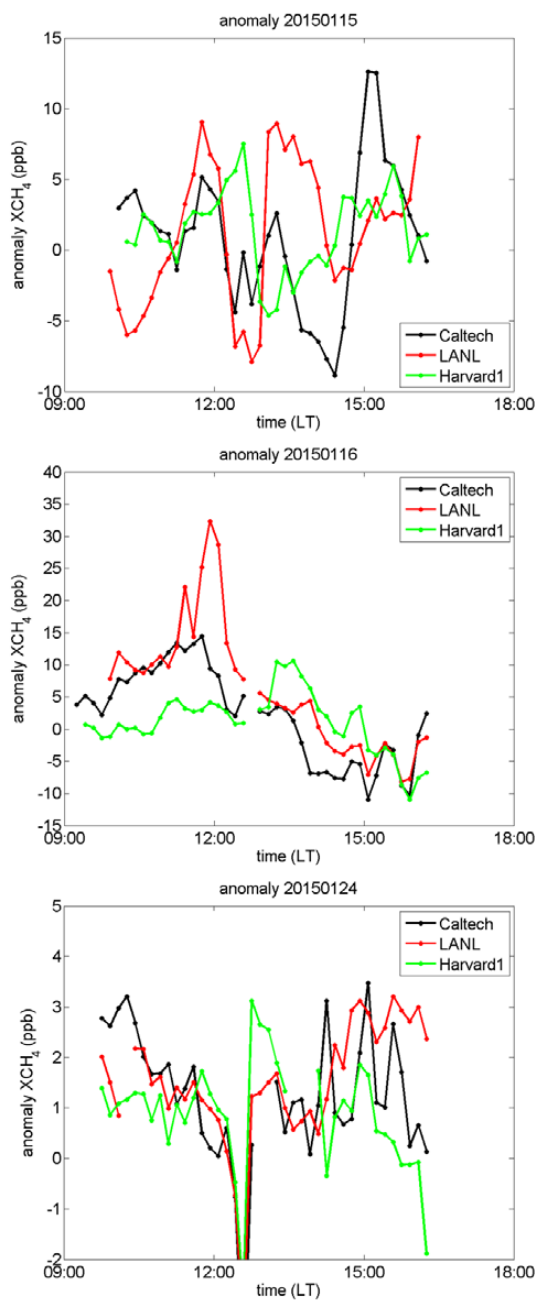
834

835 Figure 2: WRF-Chem simulation domains for the 4 grid resolutions (3-km; 1-km; 333-m; 111-m), with the
836 corresponding topography based on the Shuttle Radar Topographic Mission Digital Elevation Model at 90-
837 m resolution). The 16 rectangular areas (2 x 2 km²) are shown on the LES domain map and numerate by
838 pixel numbers (Figure 10).



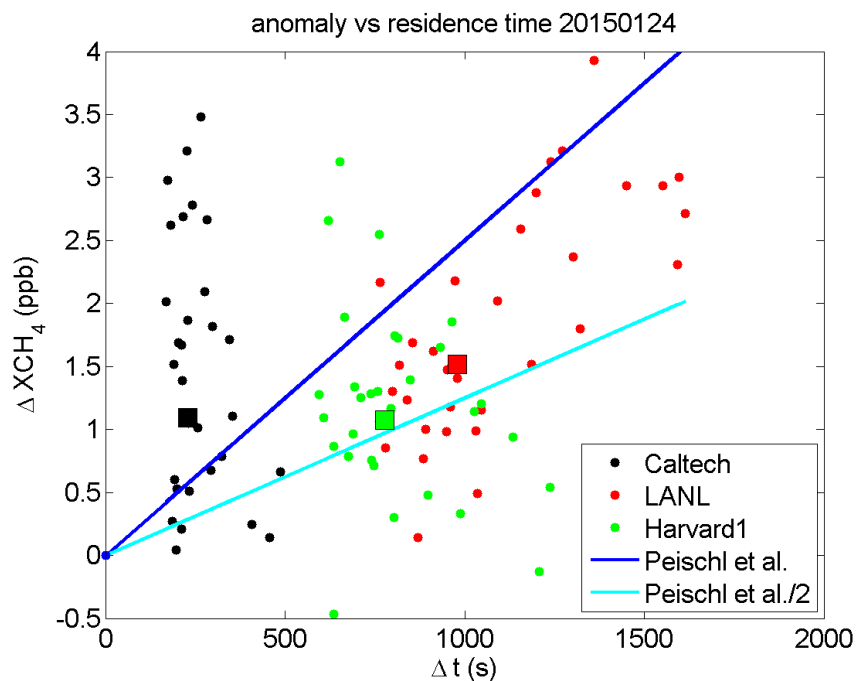
839

840 Figure 3: One minute-average time series of X_{CH_4} (upper panels a, b, and c) and X_{CO_2} (lower panels d, e, and
841 f) measured by the four EM27/SUN (black, red, green, and blue marks correspond to the Caltech, LANL,
842 Harvard1, and Harvard2 spectrometers, respectively).



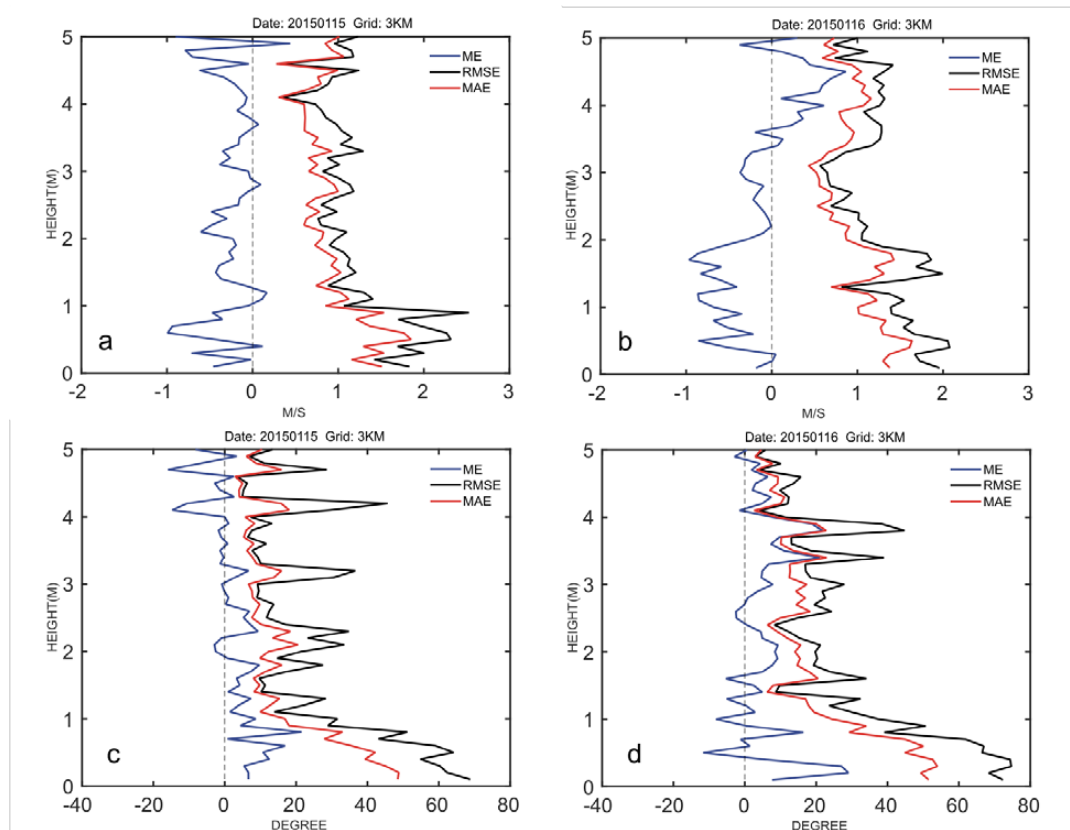
843

844 Figure 4: Time series of the 10-minute average X_{CH_4} anomaly ($\Delta_{X_{CH_4}}$, in ppb) computed relative to the
845 Harvard2 instrument for January 15th (upper panel), January 16th (middle panel), and on January 24th 2015
846 (lower panel).



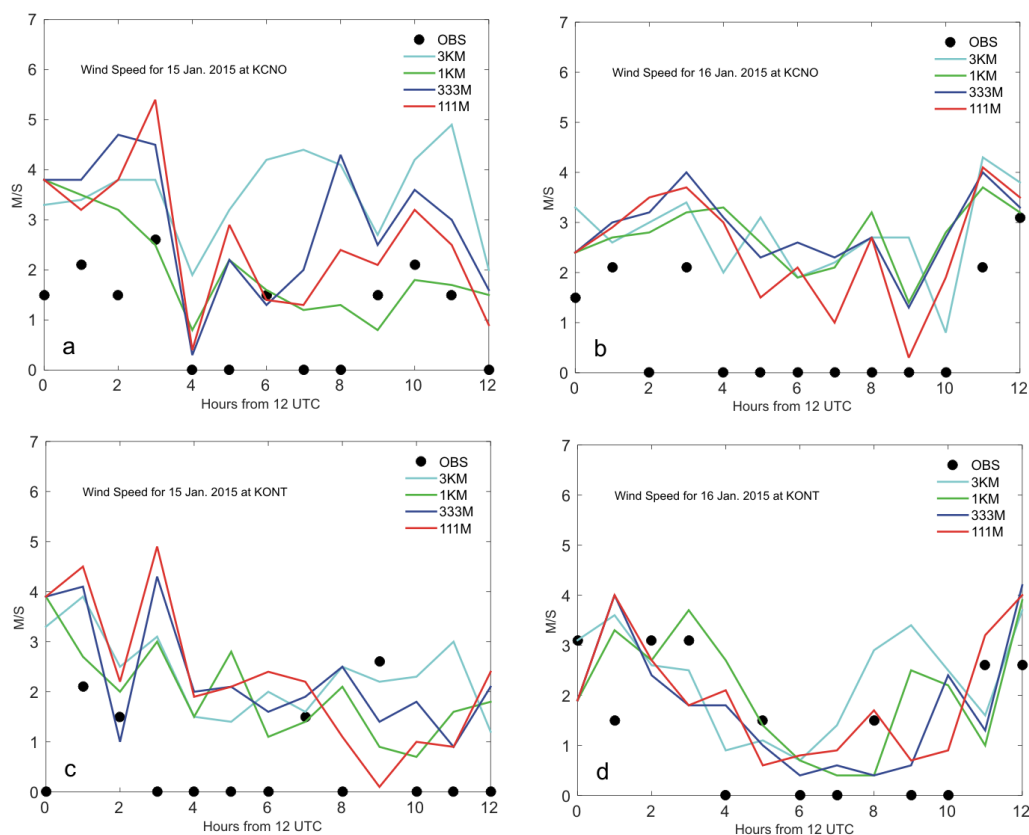
847

848 Figure 5: Estimated fluxes using FTS observations on January 24th. The 10-minute anomalies are plotted
849 against the time that air mass travelled over the dairies, so that the slopes are equivalent to X_{CH_4} fluxes (in
850 ppb/s, equation 5). The blue (and cyan) line represents the fluxes (and half of the value) estimated at
851 Chino in 2010 (Peischl et al., 2013). The squares are the medians of the data which correspond to the
852 estimated fluxes using the FTS observations (in black, red and green for the Caltech, LANL, and Harvard2
853 instruments).



854

855 Figure 6: Vertical profiles of mean horizontal wind velocity errors (upper row) and direction (lower row)
856 averaged from the WMO radiosonde sites available across the 3-km domain, with the Mean Absolute
857 Error (in red), the Root Mean Square Error (in black), and the Mean Error (in blue). Only measurements
858 from 00z radiosondes were used in the evaluation.

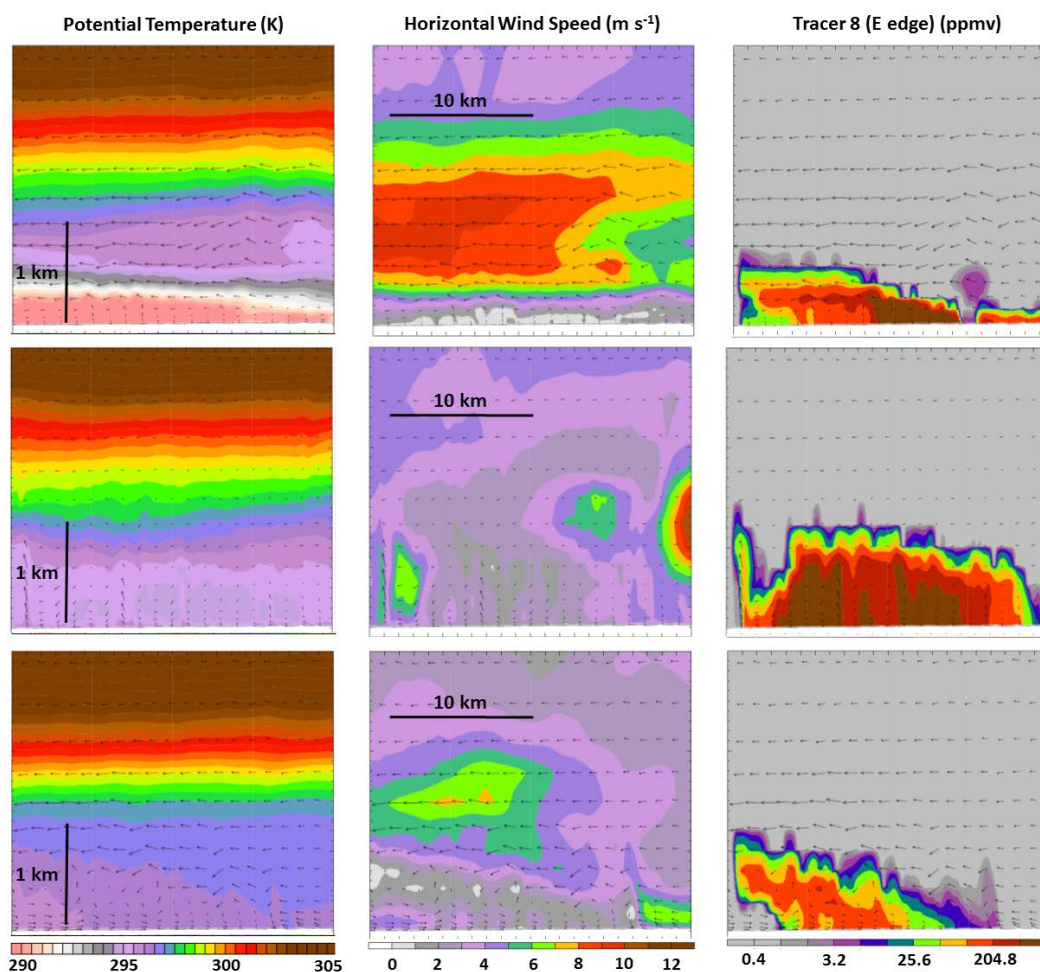


859

860 Figure 7: Mean horizontal 10-meter wind velocity in ms^{-1} measured at Chino (KCNO) and Ontario (KONT)
861 airports for January 15th and 16th (black circles) compared to the simulated wind speed for different
862 resolutions using WRF hourly-averaged results. When black circles indicate zero, the wind velocity
863 measurements are below the WMO minimum threshold.

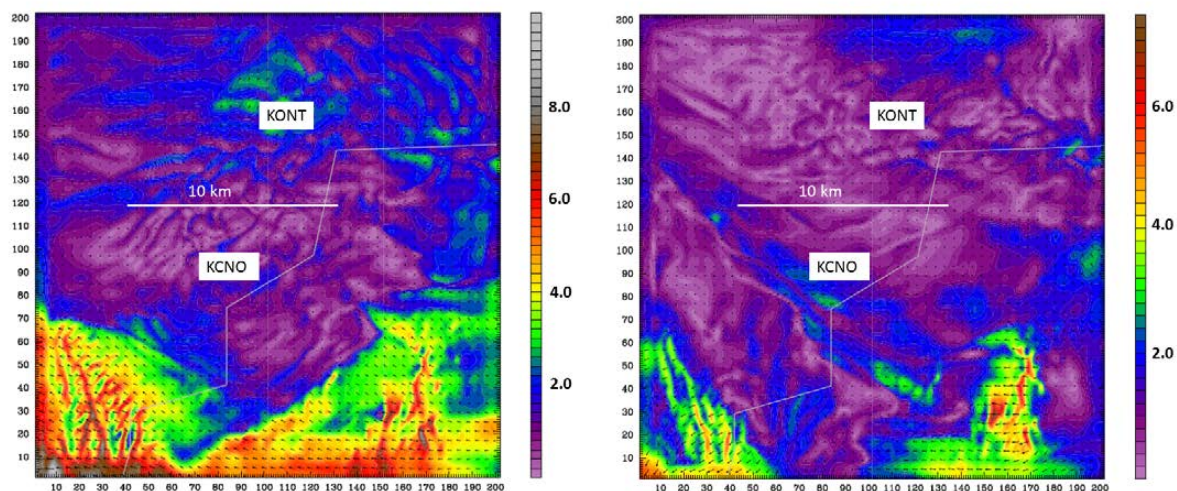


864



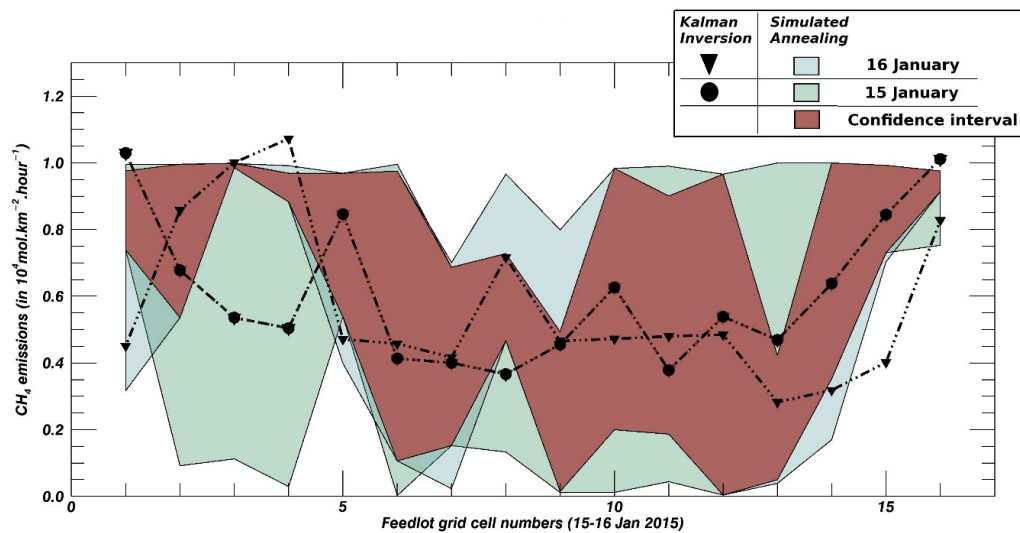
865

866 Figure 8: Vertical transects across the 111-m West-East WRF-LES simulation domain (pixels 5, 6, 7, and 8)
867 at 18:00 UTC of January 15th (upper row), 21:00 UTC (middle row), and 00:00 UTC (lower row). From left
868 to right, simulated data are shown for potential temperature (in K, left column), mean horizontal wind
869 speed and direction (in ms⁻¹ and degree, middle column), and passive tracer concentration released from
870 an eastern pixel of the emitting area (pixel 5, right column), to illustrate the relationship between the
871 three variables.



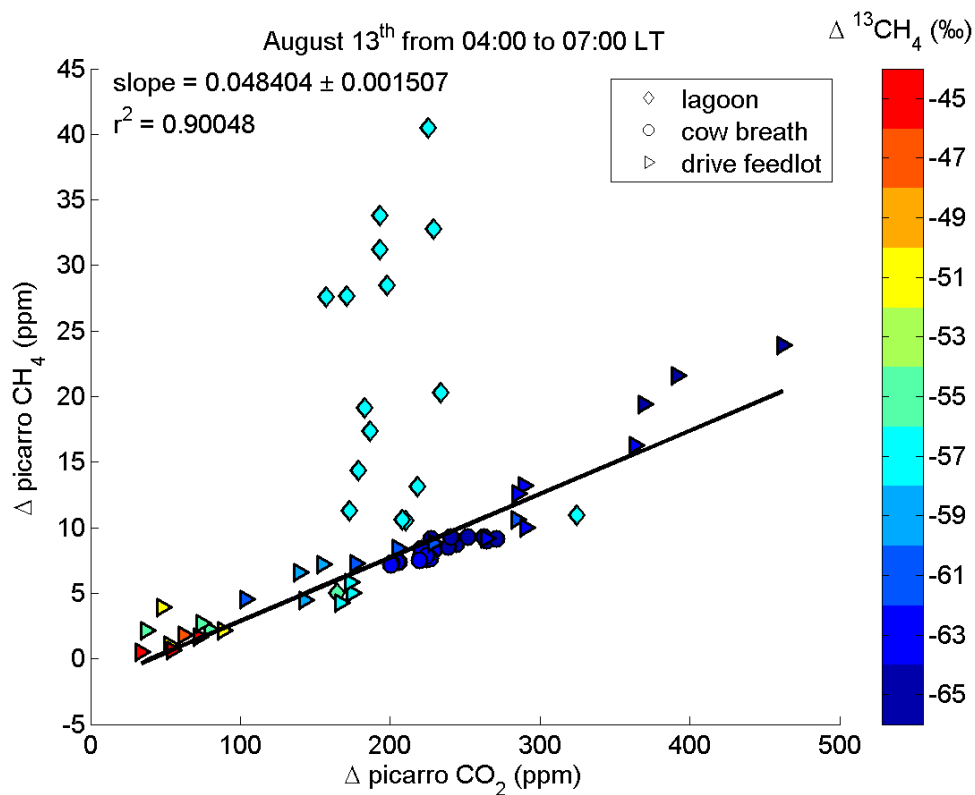
872

873 Figure 9: Mean horizontal wind field (in ms^{-1}) in the first level of the domain at 111-m resolution simulated
874 by WRF-LES for January 15th (left panel), and January 16th 2015 (right panel), at 18:00 UTC. High wind
875 speeds were simulated over the hills (southern part of the domain) whereas convective rolls,
876 corresponding to organized turbulent eddies, are visible in the middle of the domain (i.e. over the feedlots
877 of Chino), highlighting the importance of turbulent structures in representing the observed horizontal
878 gradients of CH_4 concentrations. The locations of the Chino (KCNO) and Ontario (KONT) airports and the
879 counties border (white line) are indicated.



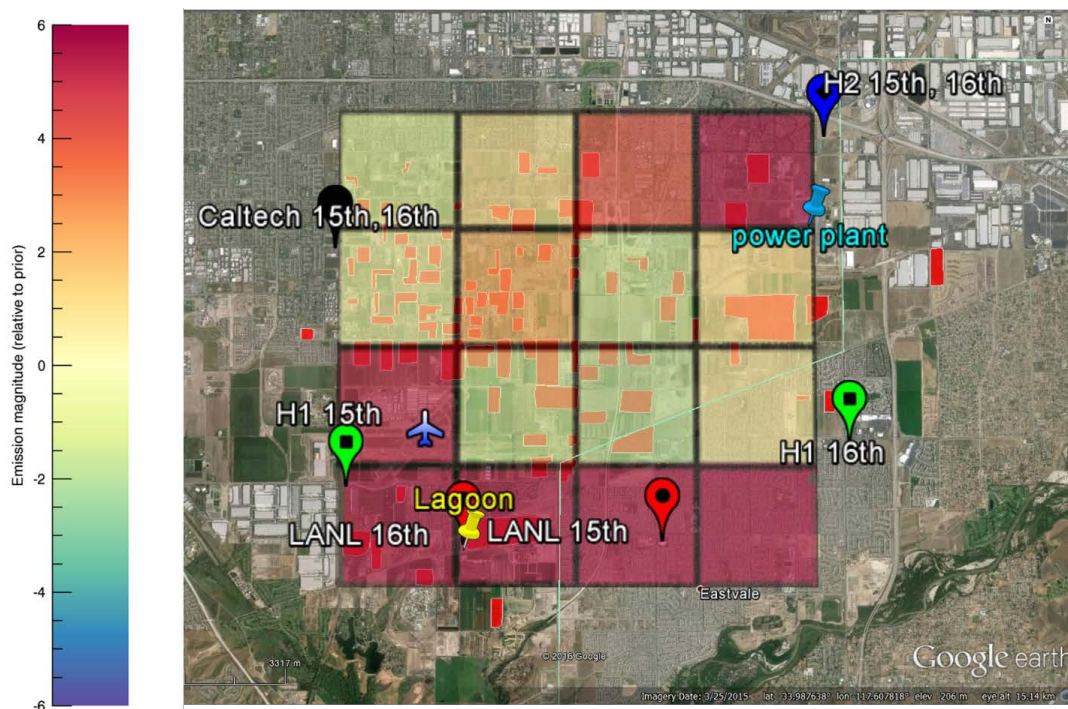
880

881 Figure 10: Emissions of CH₄ (in mol/km²/hour) for the 16 pixels (2 x 2 km² shown In Figure 2) describing
882 the dairies for both days, i.e. the 15th and 16th of January 2015. The Bayesian mean emissions are shown
883 in black (triangles and circles) whereas the colored areas represent the accepted range of solutions using
884 the Simulated Annealing technique (see section 3.2).



885

886 Figure 11: Scatter plot of one minute-average anomalies (from the 5 minutes smoothed) of CH_4 versus
887 CO_2 , color coded by the delta CH_4 values, measured by the Picarro on August 13th from 04:00 to 07:00
888 (LT).



889

890 Figure 12: Map of the *a posteriori* X_{CH_4} fluxes (mean of January 15th and 16th runs) from the WRF-LES
891 simulations, superimposed on a Google earth map, where the dairy farms are represented by the red
892 areas as shown in Figure 1. The domain is decomposed in 16 boxes (2km x 2km), in which the colors
893 correspond to the *a posteriori* emissions from the WRF-LES inversions. Red (blue) colors mean more (less)
894 CH_4 emissions than dairy cows in that box. The locations of the lagoon (yellow pin) and the power plant
895 (blue pin) are also added on the map. Map provided by GOOGLE EARTH V 7.1.2.2041, US Dept. of State
896 Geographer, Google, 2013, Image Landsat, Data SIO, NOAA, U.S. Navy, NGA, and GEBCO.